Development and Characterization of Size-controlled Non-spherical Platinum Nanoparticles as Catalyst for Proton Exchange Membrane Fuel Cells

by

Xiaoyu Tan

A thesis
presented to the University of Waterloo
in fulfillment of the
thesis requirement for the degree of
Master of Applied Science
in
Mechanical and Mechatronics Engineering

Waterloo, Ontario, Canada, 2022

Author's Declaration

I hereby declare that I am the sole author of this thesis. This is a true copy of the thesis, including any required final revisions, as accepted by my examiners.

I understand that my thesis may be made electronically available to the public.

Abstract

Platinum (Pt) nanoparticles with different sizes of 2nm and 5nm supported on functionalized high surface area carbon (HSC) have been successfully synthesized with a one-pot synthesis technique in large scale. Of the interest for the proton exchange membrane fuel cell applications, the synthesized supported catalysts are evaluated by physical characterizations, half-cell and scaled up single cell tests to study the impact of the catalyst sizes on cell performance and durability. Physical characterizations clearly demonstrate the sizes, shapes, crystallinity phases, and the total loading of the Pt nanoparticles on HSC. Half cell characterizations demonstrate higher electrochemical surface area, higher mass activity, and less durability for the working electrode prepared by the smaller Pt nanoparticle sizes (2nm) than the larger Pt nanoparticles (5nm). Scaled up single cell tests using air and hydrogen as the cathode and anode reactants demonstrate the membrane electrode assembly (MEA) prepared by smaller Pt nanoparticle sizes (2nm) shows the maximum power density of 1.1 W/cm^2, which is 7% higher than the maximum power density of MEA prepared by larger Pt nanoparticles (5nm) under similar operational conditions. The 30,000 cycles of accelerated stress test on the membrane electrode assembly prepared by larger Pt nanoparticles (5nm) demonstrates 13% drop at maximum power density, illustrating the excellent performance against degradation (ageing).

Keywords:

Pt/C catalysts; Pt particle sizes; Mass activity; Durability; Proton exchange membrane fuel cells (PEMFC)

Acknowledgements

I would like to express my deepest gratitude to my supervisor Dr. Xianguo Li for his guidance, support, and encouragement throughout my MASc degree. The lessons that I have learned from Dr. Li are not limited to the academic knowledge and to being a researcher, but also about thinking and acting like a professional engineer, which will be valuable for me throughout my career and life. life. I would also like to thank my committee members, Dr. XiaoYu Wu and Dr. Jean-Pierre Hickey for taking the time to review my thesis.

I would also like to thank Dr. Samaneh Shahgaldi for the guidance, encouragement and mostly importantly, the countless hours that we spent together working on the catalyst materials, discussing the problems and possibilities of improvements from the synthesis to the characterizations though out the time of my MASc study. Further, I would also like to thank Dr. Huiyuan Liu for answering my questions and helping me solving the issues with the half-cell tests.

Last but not least, I would like to thank my family and friends for encouraging and supporting me during my toughest time though the COVID-19 pandemic. I am especially grateful to my mother for providing me all the support I need and preparing me for my future.

Table of Contents

List of Figures

List of Tables

List of Abbreviations

ACL	Anode catalyst layer
AFC	Alkaline fuel cell
AST	Accelerated stress test
CCL	Cathode catalyst layer
CL	Catalyst layer
DI	De-ionized water
ECSA	Electrochemical surface area
EG	Ethylene glycol
FCC	Face centered cubic
GC	Glassy carbon
GDL	Gas diffusion layer
HOR	Hydrogen oxidation reaction
HSC	High surface area carbon
LSV	Linear sweep voltammetry
MA	Mass activity
MEA	Membrane electrode assembly
MCFC	Molten carbonate fuel cell
MPL	Microporous layer
OCV	Open circuit voltage
ORR	Oxygen reduction reaction
PAFC	Phosphoric acid fuel cell
PEM	Proton exchange membrane
PEMFC	Proton exchange membrane fuel cell
RDE	Rotating-disk electrode
RH	Relative humidity
RHE	Reversible hydrogen electrode
SA	Specific activity
SOFC	Solid oxide fuel cell
TEM	Transmission electron microscopy
TGA	Thermogravimetric analysis
XRD	X-ray diffractograms

List of Symbols

A	Area [m^2]
J	Current density [$A \cdot cm^{-2}$]
m	Mass [g]
υ	Potential Vs RHE [V]
v	Scan rate [$V \cdot s^{-1}$]

Greek letter

τ	Mean size of the particles
λ	Wavelength
β	Line broadening at half the maximum intensity
θ	Bragg angle

Subscript and superscript

eff	Effective
k	Kinetic
L	Limiting

Chapter 1: Introduction

The usage of fossil fuels has powered the fast growth of economies and improved the quality of lives around the globe for over a century [1]. However, due to climate change caused by the release of greenhouse gases from the usage of fossil fuels and the nature of limited supply due to depletion, fossil fuels are gradually being replaced by renewable energy sources and technologies like hydropower, biomass, geothermal, solar, wind and hydrogen fuel cells [2-4]. Hydrogen fuel cells, due to their unique advantages, can be applied to not only stationary but also mobile utilities, therefore making it a promising alternative to the conventional power sources [5]. Ever since the fuel cells powered the Apollo moon missions and the introduction of the first fuel cell vehicle by GM in the 1960s, fuel cell technologies have gradually become more and more mature, and the applications of fuel cells have been on the verge of wide commercialization and are on the upward trajectory to penetrate the market [6-8].

1.1 Hydrogen Fuel Cells: The Categorization

Depending on the criteria used, fuel cells can be classified differently. The primary categorization method uses the type of electrolyte utilized to name the fuel cells, such as proton exchange membrane fuel cells (PEM fuel cells or PEMFCs), alkaline fuel cells (AFCs), phosphoric acid fuel cells (PAFCs), molten carbonate fuel cells (MCFCs) and solid oxide fuel cells (SOFCs) [9,10]. Among those fuel cells, PEMFCs have received most efforts of research due to their outstanding features like low temperature of operation, small size thanks to using polymer membranes as electrolyte, no moving parts, easiness to stack and scale up [11].

1.2 PEM Fuel Cells: The Basics

PEM fuel cells convert the chemical energy in hydrogen and oxygen directly into electrical energy, with the only by-product of water, through a key step of oxygen reduction reaction (ORR) [6]. Figure 1 below illustrates the schematic of the symmetrically layered structure of the PEM fuel cells. From both the anode and the cathode ends towards inside, a typical PEM fuel cell consists of two flow plates and the gas diffusion layers (GDLs) for gas distribution and water removal, the catalyst layers (CLs) and proton exchange membrane in the middle. The GDL typically has a carbon-based porous structure to deliver the gas from the flow channel to the CL and transport the by-product of the reaction, water. A thin layer of microporous layer (MPL) is usually added to the GDL in contact of the CL to help the removal of excess water. The CL consists of platinum (Pt) or other active electrochemical catalyst nanoparticles, supported on a porous carbon-based substrate and covered with a thin layer of binding material. The proton exchange membrane (PEM) is a polymer electrolyte that allows the transportation of protons, while preventing the electrodes from going though due to its high electric resistance and separating the reactant molecules (H_2 and O_2) from direct contact.

When the PEM fuel cell is active, at the anode side, hydrogen molecules travel from the flow tunnels and though the anode GDL to then break into hydrogen ions (proton) and give out electrons on the surface of the Pt nanoparticles at the anode CL, though the hydrogen oxidation reaction (HOR):

$$H_2 \rightarrow 2H^+ + 2e^- \tag{1.1}$$

The protons travel through the ionomer and to the PEM to reach the cathode CL, while the electrons go though the carbon substrate of the CLs, GDLs, the flow plates and the external circuit and eventually reach the cathode CL as well, where they react with the oxygen molecules from the cathode flow channel though cathode GDL to form water and heat, though the ORR:

$$\frac{1}{2}O_2 + 2H^+ + 2e^- \rightarrow H_2O + heat \tag{1.2}$$

Thus, the overall reaction that is happening constantly inside the PEM fuel cell is:

$$\frac{1}{2}O_2 + H_2 \rightarrow H_2O + heat + electricity \tag{1.3}$$

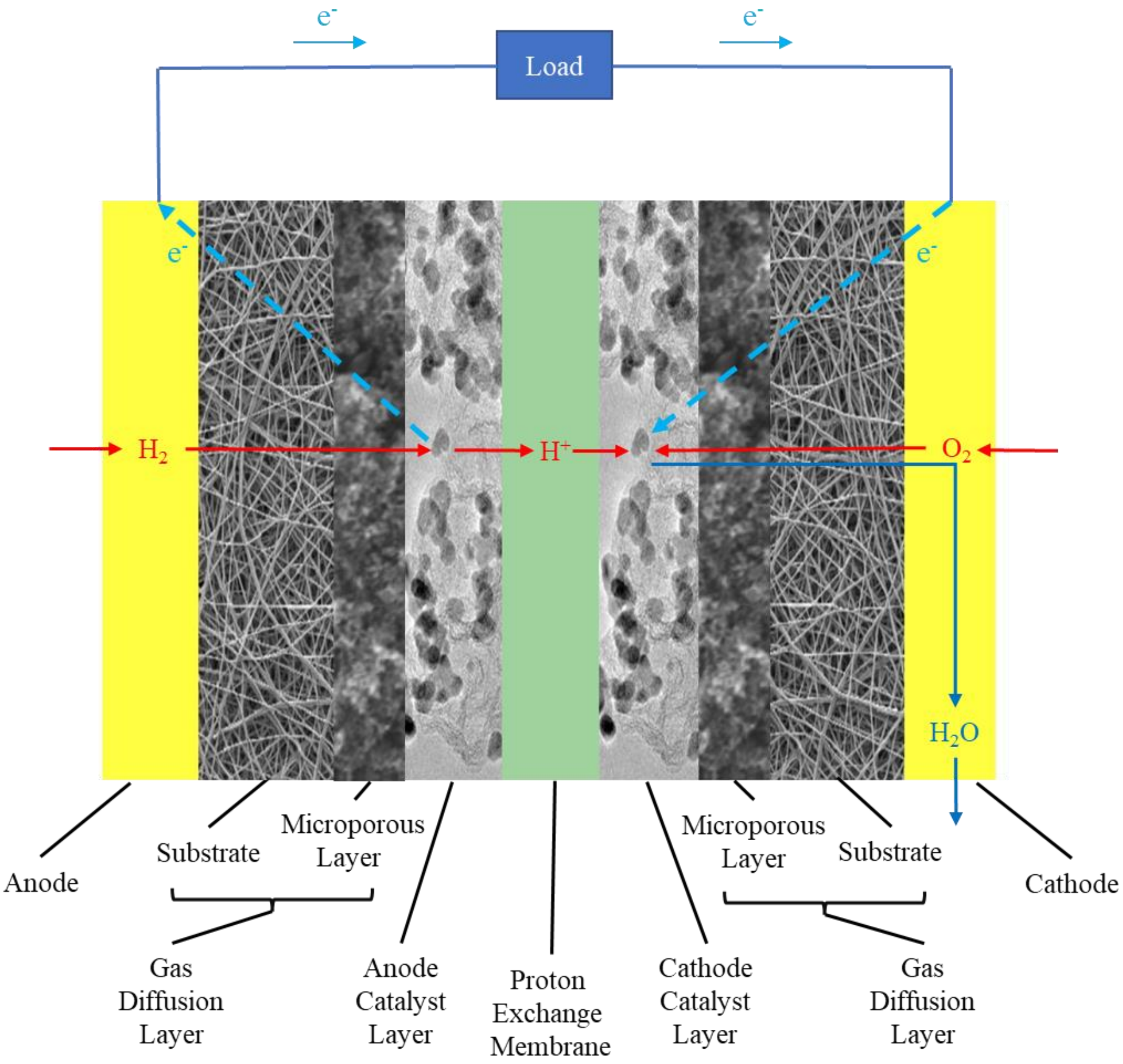

Figure 1. Schematic of PEM Fuel Cells (not to scale)

Water as a by-product of the reaction forms at the cathode CL and is constantly transported through the voids and the pores of the supporting carbon substrate in CL, then though the voids in GDL and finally leaves the cell via cathode side flow channel. Removing excess water from accumulating at the reaction sites, to prevent what is known as flooding, is important to ensure that all reaction sites can be reached by the reactants constantly, so that the cell can perform at highest efficiency. At the same time, the PEM requires certain amounts of water to exists to prevent dehydration. Therefore, maintaining water balance of the cell is important for the cell performance.

Heat produced during the reaction is generally transferred by conduction between the CL and PEM, and by conduction and convention between the CL and GDL towards the outside of the cell. Although increased cell temperature can improve the electrochemical reaction rate in the cell to some degree, membrane dehydration can occur as a result of extreme temperature, causing damage to the cell. Therefore, external cooling mechanisms such as the bipolar plate are usually used to assist the heat removal from the cell to maintain the optimal operating temperature.

1.3 Performance of PEM Fuel Cells

In PEM fuel cells, the difference of the electrical potential between the cathode, which has the higher potential from the ORR reaction, and the anode, which has the lower potential from the HOR reaction, is known as the cell potential [9]. In ideal conditions without any energy loss, the highest cell potential that the cell can achieve is 1.23 V, which is known as the reversible cell potential [9]. The reversible cell potential can be reduced to 1.19 V if the product of water if in gas form [9]. When operating, the actual cell potential is always lower than the reversible cell potential due to energy loss, the difference of which is known as overpotential [9]. The overpotential mainly comes from three sources including the loss from the sluggish electrochemical reactions known as activation overpotential, the loss from the resistance of transporting the electrons and ions within the cell known as Ohmic overpotential, and the loss from resistance of the mass transport of the reactants known as concentration overpotential.

1.4 Catalyst Layers in PEM Fuel Cells

CLs serve several roles in the PEM fuel cells. First and the key role of the CLs, is to provide the reaction sites with the electrochemical catalyst nanoparticles for the reactions to take place. The ideal operating temperature for PEM fuel cell is around 60-80°C, at which membrane has best humidification conditions for high proton conductivity [12]. However, the low temperature limits the rate for the electrochemical reactions, especially ORR [13]. Therefore, a catalyst with high electrochemical activity is required to speed up the reactions, especially for the cathode side. An ideal catalyst should allow a strong binding between the oxygen and catalyst surface, while allowing the products to freely detach from it for not blocking the reaction sites, thus achieving high reaction rate in the continuous reactions. From figure 2 below, Pt as the catalyst has highest ORR activity when compared to other metal groups. At the current state, Pt as catalyst material for PEM fuel cell are the most common and most investigated. Meanwhile, research efforts have also been put into high activity Pt, Pt alloys and other options to reduce the amount of Pt used in the catalyst to lower the material cost.

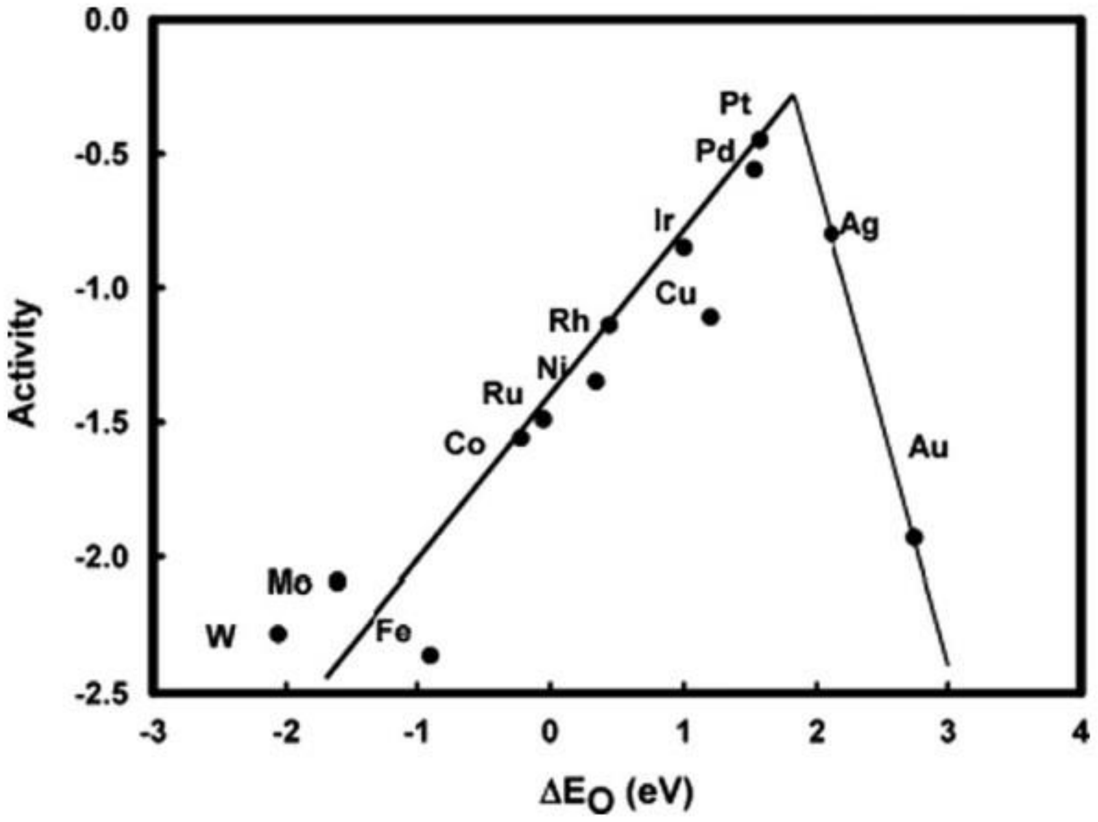

Figure 2. Oxygen reduction reaction activity v.s. the oxygen binding energy for different metals [14]

The second role of the CLs is to create bridges for the half-cell reaction products including protons and electrons between the reaction sites and the PEM and GDL respectively. The Pt nanoparticles in the CLs are usually supported by a carbon-based substrate, on which the nanoparticles are well dispersed to achieve maximum surface area. The substrate is usually made of high surface area carbon materials like carbon black (e.g. Vulcan XC-72). Because of the good electrical conductivity of the carbon material, the substrate could transfer the electrons between the Pt nanoparticles and the GDL [15].

Last but not least, the CLs deliver the reactants to and remove the products (water) from the reaction sites effectively for the continuous reactions to happen to reach high performance. This is achieved by the porous nature of the CL's structure and the hydrophobic nature of the binding material, with the pressure gradient caused by the combination of the constant back pressure of the reactant supply and the removal of the reactants at the reaction sites, and the generation of water at the cathode CL and water constantly being removed from the cathode flow channel though the MPL and GDL [16-19].

1.5 Size-controlled Pt Nanoparticles

The size of Pt nanoparticles in the catalysts can range from 1-2nm to 10+nm [20, 21]. Generally, catalysts with smaller Pt nanoparticles tend to have higher active surface area and therefore better performance. However, smaller Pt nanoparticles are also more prone to degradation effects resulting in inferior durability [22]. Controlling the factors like temperature and pH during the synthesis can directly impact the size of the Pt nanoparticles [23,24].

1.6 Shape-controlled Pt Nanoparticles

Shape controlled catalysts can expose different facets of the Pt nanoparticles and therefore alter the adsorption behavior of the reactants onto the catalyst and improve the dynamics of the ORR [25]. Different chemical and physical methods are used to control the shape of the catalyst Pt through changing the surface energy of the Pt nanoparticles in the synthesis procedure by using organic capping agents, controlling the pH and controlling the temperature [26]. In colloidal chemistry, a combination of organic surfactants and stabilizers are commonly used to control the shape of the Pt nanoparticles by absorbing onto specific facets of the crystal and therefore altering the growth rate of certain directions of the crystalline structure [27, 28]. Changing in the pH during synthesis can also impact the shape formation of the Pt nanoparticles [29].

1.7 Scope and Objectives of the Thesis

For decades, researchers have been improving the performance and durability of the PEM fuel cell, and finally the commercialization of it is on the verge. Being the most crucial and the most expensive part of the PEM fuel cell, the catalyst still has a lot of room to improve. There exists a conflict where catalyst studies for PEM fuel cell usually synthesize catalysts in small quantities in a tightly controlled environment and only analyze the ex-situ performance, e.g. measured with a rotating-disk electrode (RDE), which is measuring the stand-alone performance of the catalyst, apart from the fuel cell environment [30-33]. Compared to the actual fuel cell operating condition or the in-situ testing with a membrane electrode assembly (MEA), the RDE tests use a liquid form electrolyte, very small quantity of catalyst, and are tested on a different platform, the overall test conditions of which are considered less harsh; therefore, while the catalysts that perform well in RDE are proven to have valuable catalytic properties, the traits may not transfer to the scaled-up MEA tests [34]. This creates a discrepancy where the leading-edge catalyst technologies have difficulty to scale up for mass production at a reasonable cost while holding the performance, and the state-of-the-art commercial catalyst technology stays behind.

The objective of this study is therefore to (i) develop non-spherical high-active-surface-area Pt nanoparticles with two different sizes on functionalized high-surface-area carbon via a simple and one-pot synthesis method, which is followed by comprehensive physical and ex-situ and in-situ characterizations to (ii) elucidate the impact of Pt nanoparticles sizes on the cell performance and durability.

The thesis is divided into five chapters. In chapter one, the basics of the PEM fuel cell and the characteristics of the catalyst layer are introduced. Chapter two is a detailed literature review. In chapter three, the experimental techniques are presented, and the results of which are analyzed and discussed in chapter four. Chapter five summarizes the conclusions and the future work of the study.

Chapter 2: Literature Review

In this chapter, a comprehensive literature review is conducted with a focus on (i) the impact of carbon support, (ii) the impact of the size of the Pt nanoparticles, (iii) the impact of the shape of the Pt nanoparticles, and (iv) the impact of the synthesis techniques of the catalyst.

2.1 Impact of the Carbon Support

2.1.1 Material Selection

Various allotropic varieties of carbon have been widely and commercially used as the support material for precious metal catalysts due to its high surface area, porous nature, high electrical conductivity, the positive interactions between the support and catalyst particles and many other valuable properties [35]. Among those, carbon blacks are the most used support materials for catalyst in PEM fuel cell studies and commercial products thanks to the low cost and high availability. Carbon blacks typically consist of agglomerations of small graphite particles of near-spherical shape [36]. Table 1 below listed the common carbon black types, makers, surface area and sizes of the average carbon black particles.

Table 1. Information for commercially available carbon blacks

Carbon Black Type	Maker	Surface Area (m^2g^{-1})	Particle Size (nm)
Denka black AB [37]	Denkikagaku kogyo	58	40
Exp. sample AB [37]	Denkikagaku kogyo	835	30
Shavinigan AB [38]	Gulf Oil	70–90	40–50
Conductex 975 FB [37]	Columbian	250	24
Vulcan XC-72R FB [37]	Cabot	254	30
Black pearls 2000 FB [37]	Cabot	1475	15
3950 FB [37]	Mitsubishi Kasei	1500	16
KB EC600JD [36]	Ketjen International	1270	50
KB EC600J [36]	Ketjen International	800	50

The particle size and the nanostructure of the carbon black can affect the size of the pores of the support. If the size of the pores of the support is smaller than the size of the ionomer micelles but larger than the size of the Pt nanoparticles, some of the Pt nanoparticles can be trapped in those pores and thus not touching the ionomer, resulting in those trapped Pt nanoparticles having minimal conduction with the protons, thus increase the proton resistance and decrease their contribution to the electrochemical reaction [36]. Liu et al. [39] compared the performance of Vulcan and Ketjen black with the same ionomer to carbon ratio and same Pt loading and found out that Ketjen black has higher surface area due to larger amount of internal pores (<4nm), and the catalyst with Ketjen black as support shows 39.13% higher electrochemical surface area (ECSA) and higher cell voltage, but are more prone to voltage loss in low relative humidity (RH) conditions due to higher proton resistance in dry condition. On the other hand, Antolini et al [40] noted that the substantial amount of the internal pores of the carbon support can increase the efficiency of the fuel diffusion, while also contributing to the high dispersion of the Pt nanoparticles on the carbon support surface, the benefit of which outweighs the drawback. Therefore, high surface area carbon (HSC) is preferred as the support material for CLs in PEM fuel cells.

2.1.2 Surface Modification

Due to the inert nature of the surface of the HSC, it is usually chemically modified to interact favorably with the Pt nanoparticles and to improve catalyst dispersion [41,42]. The two major types of surface modification on carbon are nitrogen doping (N-doping) and surface functionalization with oxides. N-doping of the carbon support is to introduce nitrogen groups to the surface of the support to create a stronger bond with the Pt nanoparticles. N-doping can be achieved via in-situ methods like direct impregnation to get the exact composition of nitrogen and carbon in the support, or via ex-situ methods using pyrolysis and vapor deposition on carbon in high-temperature environment with dopants like nitrile or ammonia [43]. Yang et al. [44] reported that due to the opposite charge of the $-NH_2$ group and the ionomer, amine functionalized carbon black aggregate turned to grow much larger than untreated carbon black; moreover, the opposite charge can also improve the ionomer coverage on the surface of the support, but the experimental data is not provided. Despite the increase in power density, Fang et al. [45] observed significant carbon corrosion loss from the N-doped samples after only 500 cycles for the carbon durability test, especially with the N-doped Ketjen black, due to the Pt catalyst accelerating the breaking of the weaker covalent bound of the phenyl-amine groups prior to the carbon black, resulting in the reduced performance of the sample afterwards due to factors like detachment of ionomer.

Compared to N-doping, surface functionalization with oxides alters the surface chemistry of the support by introducing oxygen complexes using oxidants though acid treatment or with ozone and plasma [41,46,47]. The added oxygen functional groups can not only anchor the Pt nanoparticles, but also positively affect the adsorption of the Pt nano particles on the surface of the support [48]. Due to the hydrophilic nature of the added oxygen functional groups, the functionalized carbon can disperse more evenly during the synthesis process compared to untreated carbon black [49]. By using combinations of hydrochloric acid, nitric acid, and sulfuric acid to functionalize the carbons, Guha et al. [41] found out that the degree of surface functionalization determines the deposition of the Pt nanoparticles, and mild reducing agents in combination with the functionalized carbons advocate the homogeneous distribution of the Pt nanoparticles on the carbon surface.

2.2 Impact of the Size of the Pt Nanoparticles

2.2.1 Impact on Performance

Since catalyzed reaction such as ORR occurs at the catalyst surface, traditional approach is to make the Pt particles smaller so that for a given amount of Pt mass, the active surface area of the Pt is substantially increased, hence the mass activity (MA, activity on a per unit mass of Pt basis) can be improved [50]. Nesselberger et al. [31] tested a series of different sizes of Pt nanoparticles ranged from 1nm to 5nm supported on the HSC for ORR activities using half-cell tests and observed the trend of decreasing in ECSA and MA as the particle size is increased. However, if the nanoparticle sizes are too small, it can counteract the advantages of the increased surface area due to blockage of the reaction sites due to adsorption of competing molecular species [51]. Pt nanoparticles with the size ranged from 2nm to 4nm are reported to have the highest mass activity for ORR [52]. After comparing the performance of a series of Pt nanoparticles sizes from 1.6 nm to 2.6 nm, Wikander et al. [17] concluded that there is no apparent relation between the particle size and the ORR performance within the tested particle size range in half-cell tests; however, their impact in single cell and durability was not investigated.

2.2.2 Impact on Durability

As shown in Figure 3, degradation of the catalyst layer primarily appears through agglomeration, dissolution, and detachment of Pt nanoparticles through operation, resulting in reduction in ECSA, which leads to decreased performance of the fuel cell [9, 53]. The agglomeration of the Pt nanoparticles, also known as the growth and sintering of the nanoparticles, is the primary reason for the drop in ECSA [54]. One reason for the agglomeration happening is that during the operation of the fuel cell, smaller Pt nanoparticles tend to dissolve into the electrolyte and then redeposit onto larger Pt nanoparticles, causing the size of the Pt nanoparticles to grow/cluster, the process of which is known as “Ostwald ripening”. The solubility of Pt ions is strongly dependent on the potential of the electrodes; the Pt dissolution-redeposition is most active when the electrode is over 0.8 V vs. the reversible hydrogen electrode (RHE) [55]. Guilminot et al. [56] detected the existence of dissolved Pt ions in aged PEM fuel cell membranes, providing evidence for the Ostwald ripening process, while also indicating Pt complexes can transport through the membrane due to chemical diffusion and electro-osmotic drag. Xie et al. [57] found dissolved Pt species from the cathode outlet (around 100 pg per 1g of water), indicating not all dissolved Pt nanoparticles re-deposited, resulting in Pt loss over time. Another mechanism for the Pt agglomeration is through diffusion and precipitation of the Pt nanoparticles across the support surface, the process of which is independent of the electrode potential and can be observed when the potential is between 0.1 V to 0.8 V vs. RHE [58]. The Ostwald ripening and Pt diffusion/precipitation together cause Pt nanoparticles to increase in size over time; however, it remains unclear which mechanism contributes more to the result [59].

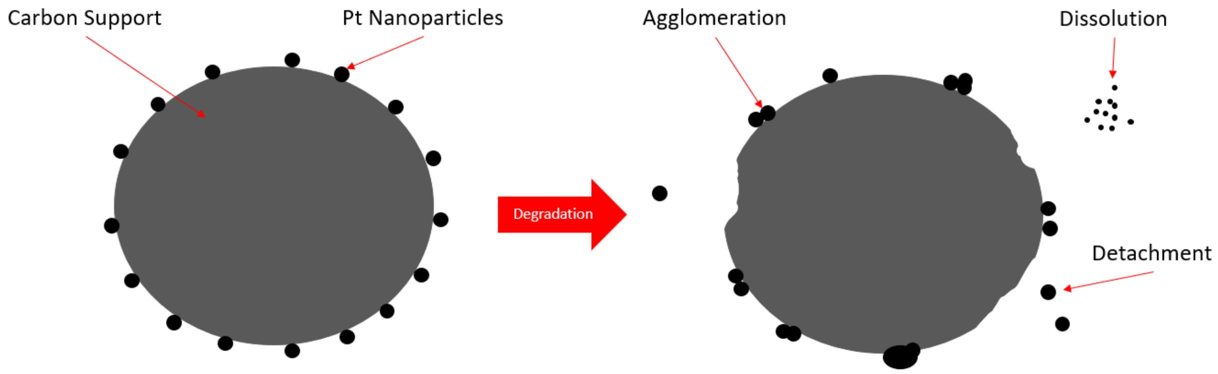

Figure 3. Degradation mechanisms of the catalyst layer

Based on the previous studies, smaller nanoparticles are found to be more prone to size growth during operations which is due to high specific surface energy of nanoparticles [60,61]. Holby et al. [30] analyzed the impact of Pt nanoparticle size on the stability of the catalyst via half-cell tests and simulations and concluded that increasing size of the Pt nanoparticles will drastically improve the stability of the catalyst. Borup et al. [62] found that the growth rate of the size of the Pt nanoparticles is accelerated by high cycling potentials under high relative humidity (RH), which leads to lower ECSA. Xu et al. [22] tested the stability of the Pt nanoparticles sized from 2.9 nm to 6.5 nm via in situ electrochemical test in a single-cell setup with an active area of 5cm^2

for up to 1300 driven potential cycles between 0.6 V and 1.2 V, and the results demonstrate that larger Pt nanoparticles have reduced surface defects which improve the durability of the electrocatalysts. However, a recent study by Yano et al. [33] reported that the durability of Pt nanoparticles on carbon support is almost independent of the particle size if the particles are evenly dispersed and the size is uniform (with standard deviation smaller than 10%) by comparing carbon supported Pt nanoparticles of size 2nm and 4nm before and after 30,000 cycles between 0.6 V and 1.0 V vs. reversible hydrogen electrode (RHE) using half-cell tests. Despite the research effort on the performance of the Pt nanoparticles of different sizes, there are many discrepancies in literature and few studies focused on the impact of Pt nanoparticles sizes on durability of the catalyst layer via scaled up single cell test. As a result, a comprehensive analysis including both half-cell and full-cell characterization would be important to fully understand the impact of the size of the Pt nanoparticles on PEMFC's overall performance and durability.

2.3 Impact of the Shape of the Pt Nanoparticles

2.3.1 Impact on Performance

The state-of-the-art Pt catalyst in PEM fuel cells consists of spherical-shaped Pt nanoparticles, the shape of which is naturally favored in the thermodynamics of the fabrication process [63, 64]. The spherical-shaped Pt nanoparticles are usually bounded by low-index planes like (111) and (100). Among the three low-index crystal planes of a face-centered-cubic (fcc) Pt nanoparticle (i.e., (100), (110), (111)), plane (111) is usually the most dominant due to the lowest surface energy, and plane (110) has the highest surface energy of all three [65]. Common shapes of Pt nanoparticles include tetrahedron (enclosed in (111) facets), octahedron (enclosed in (111) facets) and cube (enclosed in (100) facets) [66]. Shape-controlled Pt nanoparticles can deliver superior catalytic activities from selected crystal facets, particularly from the high-index planes that have higher surface energy [67]. Quan et al. [68] compared the noble metal nanocrystals with high-index planes and low-index planes, and concluded that the high-index facets of the nanocrystals are related to the higher electrochemical activities. Tian et al. [69] synthesized tetrahexahedral Pt nanocrystals, which includes 24 high-index facets like (730), (310) and (210), from electro-chemically treating spherical Pt nanoparticles using a square-wave potential combined with acids; the tetrahexahedral Pt nanoparticles achieved up to 400% electrochemical active surface area of the spherical Pt nano particles.

2.3.2 Impact on Durability

With the higher catalytic performance of the Pt nanoparticles bounded by high-index facets, it is important for the Pt nanoparticles to retain their shape and facets intact though out the operation to achieve high durability. However, due to the high-surface-energy nature of the high-index facets, during the operation of the fuel cell, the Pt nanoparticles tend to evolve into a more thermodynamically stable form. Lee et al. [70] synthesized Pt nanodendrites of size 20 to 30nm supported on carbon, and tested the catalyst in MEA environments. After 20,000 cycles of the accelerated durability test, the nanodentritic shape of the Pt was lost from TEM observations, and the ECSA decreased by 33.3% while power density at 0.6 V cell potential reduced by 59.5%, indicating the performance drop is also connected to other factors than only the active surface area loss, including the change of morphology of the Pt nanoparticles. Huang et al. [71] found that Pt crystals enclosed in high-index facets are more stable and resistant to shape transformation under extreme temperature variations compared to those enclosed in low-index facets. Huang et al. used simulation to conduct a stability test by varying the temperature from 0 to 2200K on six special shaped Pt nanocrystals that are each bounded with single type of facets, including three with low-index facets i.e., cube with (100), dodecahedron with (110), octahedron with (111), and three with high-index facets i.e., tetrahexahedron with (310), trapezohedron with (311), trisoctahedron with (331) and found the Pt nanocrystals enclosed in high-index facets retained their shape better compared to those in low-index facets. Although recent studies have investigated the performance of the shape-controlled Pt catalysts, there are very limited number of reports on the impact of the shaped Pt nanoparticles on the durability of the catalyst, especially in the fuel cell environment. Due to the harsh requirement in the synthesis procedure to get the high-index facets, shaped Pt catalyst is usually prepared in small quantities, which is usually not enough amount for MEA/fuel cell test. Therefore, a more practical and simplified fabrication process for mass production of shaped Pt catalysts would promote further investigation on their impact on the durability of the fuel cell.

2.4 Impact of the Synthesis Techniques

The synthesis process of the catalyst has significant impacts on the size and shape of the Pt nanoparticles, and the dispersion of the Pt nanoparticles on the supports [72-74]. The state-of-the-art of Pt catalyst on carbon support is synthesized via different methods like impregnation-reduction, microemulsion, ion exchange, sputtering, polyol and many others [75]. Conventionally, the Pt nanoparticles are synthesized first, and then deposited on the carbon-based substrate through various techniques during the fabrication of the Pt-based catalysts [76, 77]; this two-step process increases the complexities of catalyst fabrication and limits the rate, and hence increases the cost of catalyst production [78]. It would be preferred if the Pt-based catalysts can be produced in a simple one-step process to reduce the cost of the catalyst production.

2.5 Summary

It is conventional that most of the catalyst development is based on the half-cell characterizations or in some cases for the novel shape-controlled catalysts, the catalysts are analyzed individually, without a support or ionomer. It is also known that the good characteristics of the electrocatalyst alone or exhibited in half-cell tests often do not necessarily carry over in full cell tests. This is because the half-cell characterizations of the catalysts provide the electrochemical properties of the catalyst materials, while the full cell test results reflect the overall balance between the electrochemical kinetics and transport phenomena occurring in the catalyst layers of the cell. Whereas the catalyst layers consist of not only supported catalyst particles on which catalyzed electrochemical reactions occur and through which electron transports, but also ionomer thin film covering the catalyst surface to form the three-phase boundary and through which proton transports, and porous region among the catalyst agglomerate structures for reactant transport and product removal. In this study, none-spherical high-surface-area Pt nanoparticles of different sizes supported on HSC are synthesized via a simple and one-pot synthesis method, and the viability of the produced catalyst for large sized fuel cells for practical applications is demonstrated. The results obtained are used to explain the discrepancies in literature and contribute to the development of the practical catalysts for commercial fuel cells.

Chapter 3: Experimental Techniques

3.1 Carbon Support and surface functionalization

In a typical carbon support functionalization setup, 6 g of HSC is mixed with 800 ml of 2.5M hydrochloric acid (HCl) and refluxed at 120°C for 18 hours. The sample is then separated using centrifugal separator to collect the HSC. The collected sample is then washed with de-ionized water several times until reaching neutral pH. Next, the collected sample is mixed with 800 ml of 4 M sulfuric acid (H_2SO_4) and 4 M nitric acid (HNO_3) with volume ratio1:3, heated at 120°C for 4 hours for further functionalization. The functionalized HSC is collected after the sample is washed to neutral pH with de-ionized water (DI) using the same centrifugal separation methods.

3.2 Synthesis of Pt nanoparticles onto the functionalized High-Surface-area Carbon (HSC)

As shown in Figure 4 below, the synthesis is achieved using one-pot method, where the Pt nanoparticles deposit directly onto the functionalized HSC. First, 0.4g of the functionalized HSC is mixed with DI and Ethylene Glycol (EG) as the solvent and the reducing agent. Afterward the Pt precursor, hexachloroplatinic acid (H_2PtCl_6), is added to the solution under nitrogen, while the solution is being mixed using the magnetic stirrer bar. The pH of the solution is set to 10 using sodium hydroxide (NaOH), and the temperature is increased to 160°C or 180°C for controlling the size of Pt nanoparticles. The solution is held at the required temperature for 3 hours and afterwards the pH is decreased to 2 using HCl. Synthesized Pt/C is then collected using centrifugal separator and washed with DI water several times until pH neutral. The final product is dried under Ar atmosphere at 70°C for 24 hours.

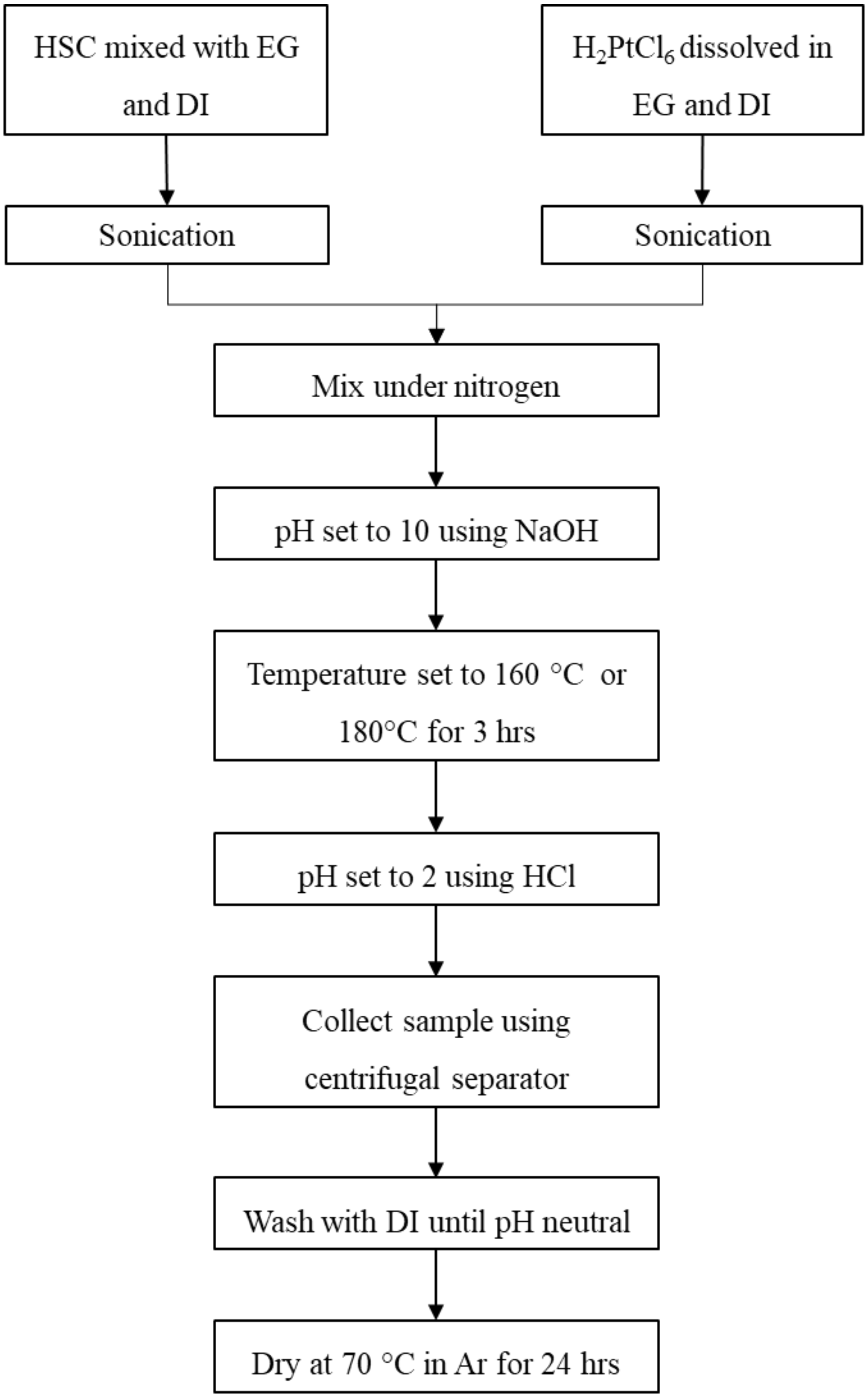

Figure 4. The one-pot synthesis procedure

3.3 Physical characterizations

3.3.1 Thermogravimetric Analysis (TGA)

The TGA is used to determine the exact Pt loading (weight percentage of Pt) of the samples. By increasing temperature of the samples from room temperature to 800°C under air flow, most of the carbon is burnt off except impurities. To calculate the exact weight of Pt, the carbon is first tested in TGA separately as the baseline to obtain the weight ratio of the impurity residual of carbon; by eliminating the residual of the impurity in carbon from the sample, the ratio of the remaining weight to the total weight of the sample is the Pt loading.

3.3.2 X-ray diffractograms (XRD)

The XRD is commonly used to determine the crystallographic structure of the material by measuring the scattering angle and intensity of the X-ray from irradiating the sample. The XRD of the samples are recorded for the 2θ angle region to determine the crystallite planes of the Pt nanoparticles.

3.3.3 Transmission Electron Microscopy (TEM)

The sample images are captured using TEM operating at 300kV with magnification between 2250x to 360kx to observe the dispersion and size of the Pt nanoparticles synthesized.

3.4 Ex-situ electrochemical characterizations

All the half-cell electrochemical measurements are carried out using CH-Instruments 760E Bi-potentiostat coupled with BAS RRDE-3A rotating disk electrode system as shown in Figure 5.

Glassy carbon (GC) disk with 4 mm diameter is used as working electrode, the reversible hydrogen electrode (RHE) is used as reference electrode and a platinum wire is used counter electrode. 0.1 M perchloric acid ($HClO_4$) saturated with N_2/O_2 is used as electrolyte. The catalyst ink is prepared using 5 mg of catalyst in 5 ml of de-ionized (DI) water, ethanol mixture in the ratio 1:9 by percentage and 30 µL of ionomer. The suspension is sonicated until homogenous dispersion of ink is formed. The working electrode is prepared by polishing glassy carbon disk with alumina slurry on a fiber pad, followed by thorough rinsing with DI water and air drying. A total of 6.4 µL aliquot of ink (containing 6.4 µg of catalyst) is drop casted onto the GC disk to make a uniform catalyst layer. The electrolyte is purged constantly with nitrogen gas for an hour to remove air from it prior to the cyclic voltammetry measurements and similarly purged with oxygen gas prior to linear sweep measurements. Durability studies for half-cell, or half-cell accelerated stress tests (AST), is carried out by cycling the potential of the working electrode between 0.5 V to 1V Vs. RHE at the scan rate of 0.5 V/s for 3,000 cycles.

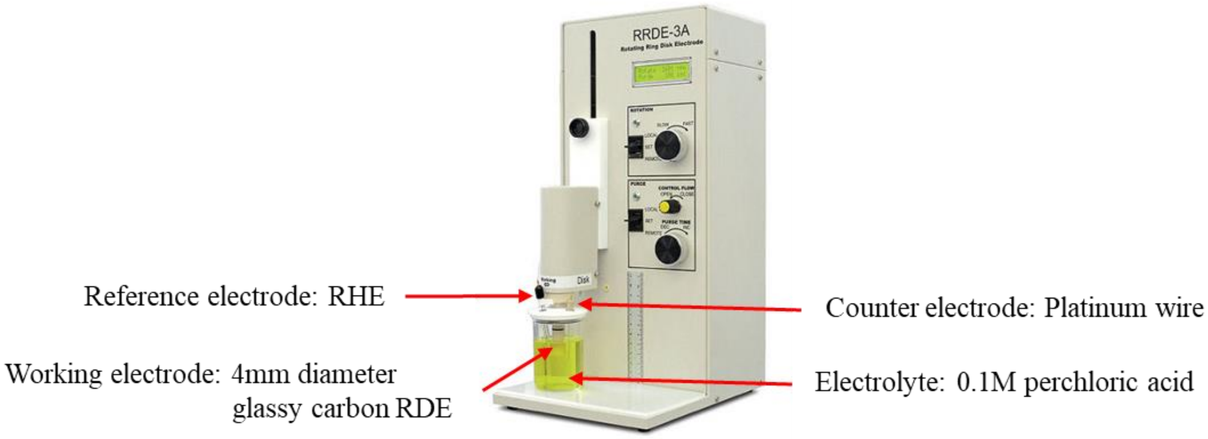

Figure 5. BAS RRDE-3A rotating disk system used for the ex-situ electrochemical characterization

3.5 In-situ electrochemical characterizations

A homogeneous ink is made by mixing the synthesized Pt/C catalyst with an ionomer, DI-water and iso-propanol. Afterwards the ink is sonicated for 1 hour, then sprayed onto both surfaces of a membrane until the proper loadings are obtained. The catalyst loading in the anode and cathode sides are set at 0.1 and 0.4 mg/cm^2, respectively, while the Pt/C to ionomer ratios are set at 3:1 for both sides. The membrane coated with catalyst layers is sandwiched between the gas diffusion electrodes and sealed with Kapton gaskets. The active surface area of the fabricated membrane electrode assembly (MEA) is 45 cm^2. The prepared MEA is placed between two straight flow-field plates and compressed to ensure proper sealing with no leakage from either side. To assess the cell performance, three flow conditions of the reactants are applied: low flow for the flow of hydrogen and air with stoichiometries of 1.2 to 2, moderate flow for the flow of hydrogen and air with stoichiometries of 1.2 to 4, and high flow for a constant flow rate of hydrogen and air at 4.45 and 9 slpm respectively. The cell backpressure and temperature are set at 35 kPag and 75°C, respectively, for both flow conditions. In addition, the behaviour of catalysts is evaluated under high (100%) and low (40%) relative humidities (RH). AST is carried out by cycling the cell voltages between 0.60 and 1 V for 30,000 consecutive cycles, at a scanning rate of 0.05 V/s. Compared to the half-cell AST, which is used a preliminary screening tool for durability analysis, the single-cell AST uses a slower scanning rate and has more cycles. After finishing the AST, the polarization curves are plotted under high (100%), and low (40%) RHs at the constant temperature of 75°C and with back pressure of 35 kPag. Electrochemical impedance spectroscopy (EIS) is measured before and after the AST at the cell voltage of 0.70 V, direct current with the amplitude of 10 mA, and frequency range of 100 mHz and 100 kHz.

Chapter 4: Results and Discussion

In this study, two sizes of Pt nanoparticles supported on HSC are obtained via controlling the one-pot synthesis reaction temperature. Figure 6 (a-c, e-h) shows the TEM images and size distribution of the as-prepared Pt nanoparticles on HSC with two different sizes. As is clear from Figure 6 (a and e) Pt nanoparticles are uniformly dispersed on the HSC support without any noticeable agglomeration and increasing the reaction temperature results in smaller Pt nanoparticles. Figure 6 (b and f) demonstrate higher magnification of TEM images for both samples, which clearly show the size differences between the prepared catalysts. In the fast nucleation growth when the reaction temperature is high at 180°C, the average particle size is around 2 nm (Figure 6 (c)); hence it is referred to as the catalyst HSC-Pt2 hereafter. At a lower reaction temperature of 160°C, the average particle size is about 5 nm, which is referred hereafter as HSC-Pt5 (Figure 6 (g)). It is clear from the high magnification TEM images (Figure 6 (c and g)) that the shape of Pt nanoparticles is also impacted by reaction temperature; for instance, at the higher temperature of 180°C all the nanoparticles are faceted, and at the lower reaction temperature of 160°C they are almond and flat shapes. Higher magnification images are taken of the nanoparticles located on the carbon edges to gain better and clearer images about the shape of nanoparticles and the impact of carbon on Pt nanoparticle shapes. To obtain the size distributions of the prepared Pt nanoparticles on HSC, two size distribution histograms are plotted which are shown in Figure 6 (d and h) related to the HSC-Pt2 and HSC-Pt5, respectively. As Pt nanoparticles are not spherical, the diameter (D_{eff}) is measured by taking the average of the lengths across (d_1) and along (d_2) the elongated direction.

$$D_{eff} = \frac{1}{2}\,(d_1 + d_2) \tag{4.1}$$

Based on histograms the average particle size is estimated to be around 2.49 nm for HSC-Pt2 and 5.19 nm for HSC-Pt5. In order to obtain the accurate Pt loading on the support, the thermogravimetric analysis (TGA) is conducted on both samples. Based on the TGA results, HSC-Pt2 and HSC-Pt5 present around 45.4% and 47.6% Pt loading, respectively.

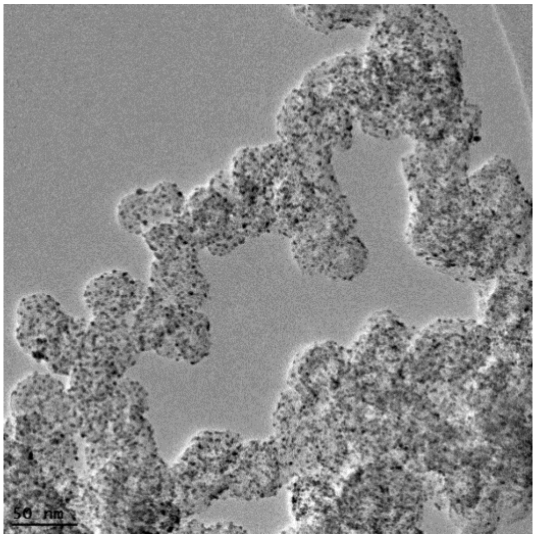

(a)

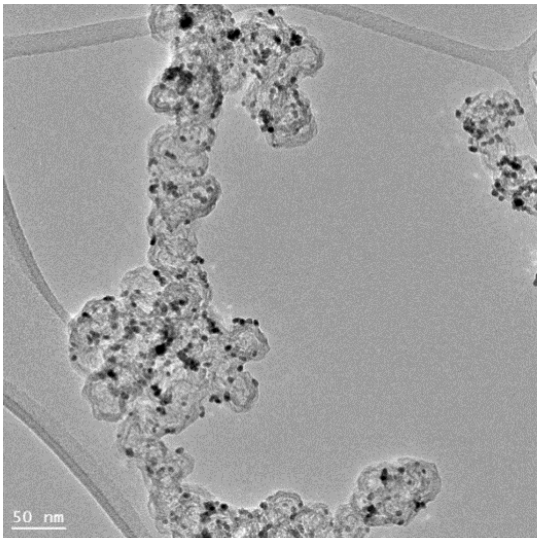

(e)

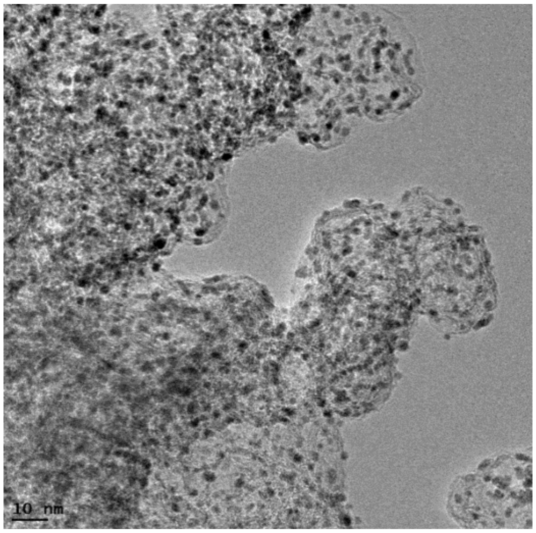

(b)

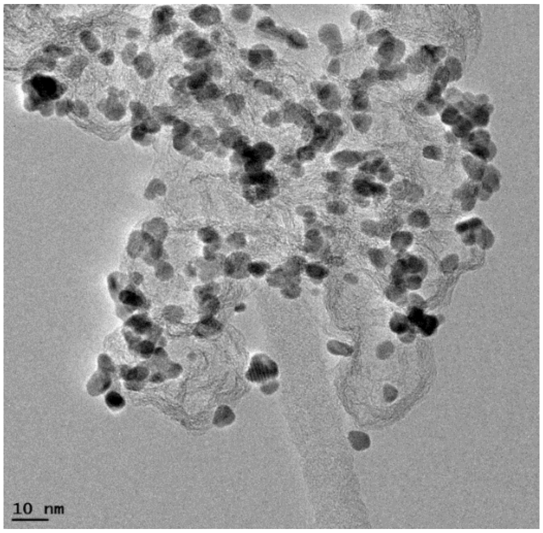

(f)

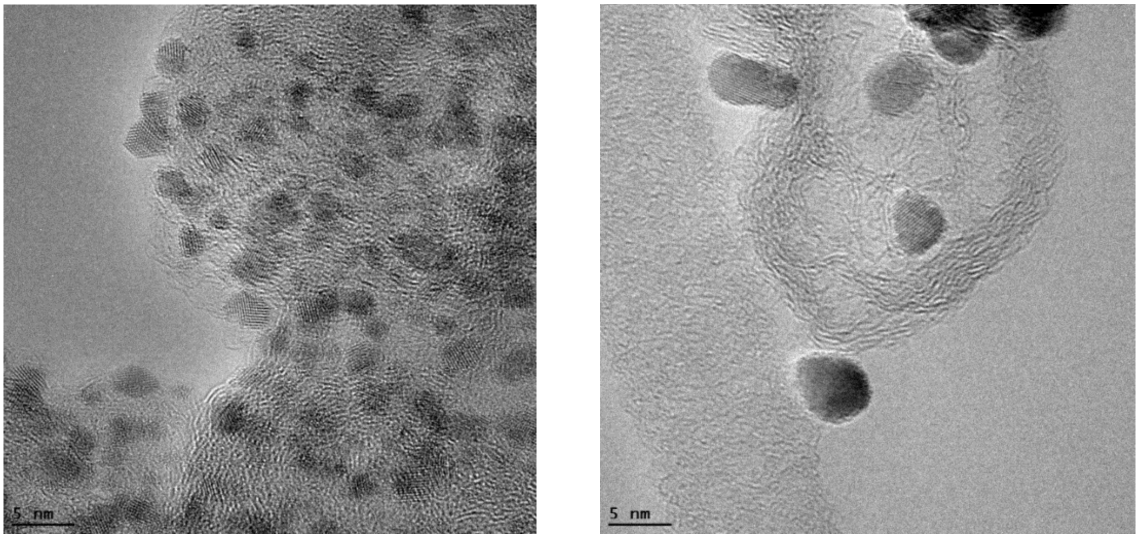

(c) (g)

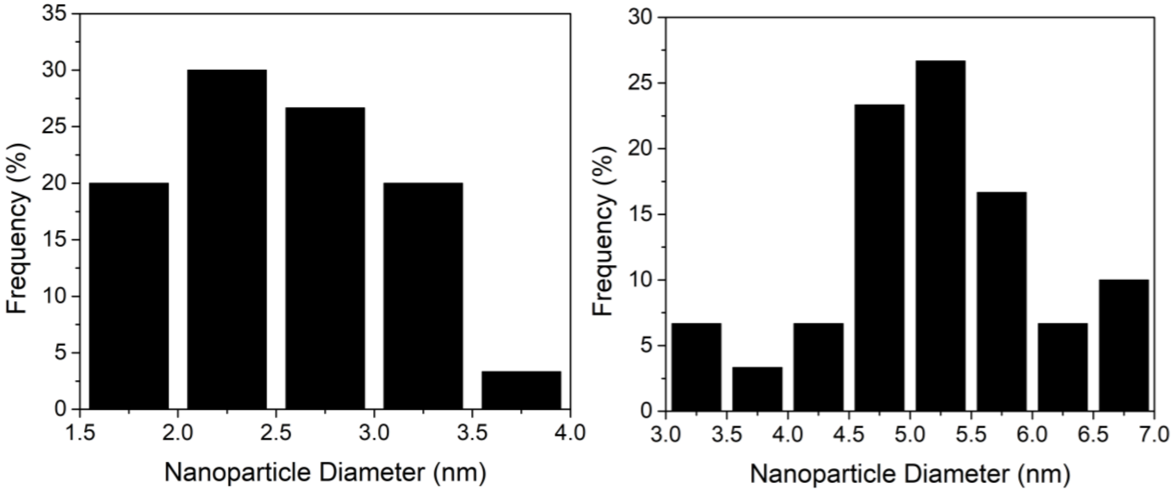

(d) (h)

Figure 6. TEM images of the synthesized HSC-Pt at the reaction temperatures of 180°C (a-c) and 160°C (e-g) at the different magnifications, and the Pt nanoparticle size histograms related to the reaction temperature of (d) 180 °C, and (h) 160 °C.

Figure 7 presents the XRD pattern of the synthesized HSC-Pt2 and HSC-Pt5 catalysts, illustrating the characteristics of the property of the crystalline Pt face's centered cubic (fcc) phase. The peaks are located at 40°, 46.5°, 67.9°, 81.6°, and 86.3°, and are assigned to (111), (200), (220), (311), and (222) crystallographic planes, respectively. XRD peaks of the synthesized HSC-Pt2 and HSC-Pt5 are comparable with those corresponding to bulk Pt and commercial Pt/C catalysts reported in literature [79]. The XRD results indicate more high-index facets like (311) in both samples compared to the Pt nanoparticles from literature, while HSC-Pt5 shows higher portion of the high-index facets with higher intensity peaks at the corresponding 2θ angle compared to HSC-Pt2. Based on the Debye-Scherrer equation, the particle sizes of HSC-Pt2 and HSC-Pt5 are estimated as, respectively, 3 nm and 5nm, which are almost consistent with the observations from the TEM images as well.

$$\tau = \frac{0.9\lambda}{\beta \cos\theta} \tag{4.2}$$

where τ is the mean size of the particles, λ is the wavelength of the X-ray, β is the line broadening at half the maximum intensity (FWHM) and θ is the Bragg angle in the Debye-Scherrer equation. Therefore, the particle sizes estimated from the TEM images are considered as more reliable, while XRD results provide a good confirmation of the Pt particle sizes estimated from the TEM images.

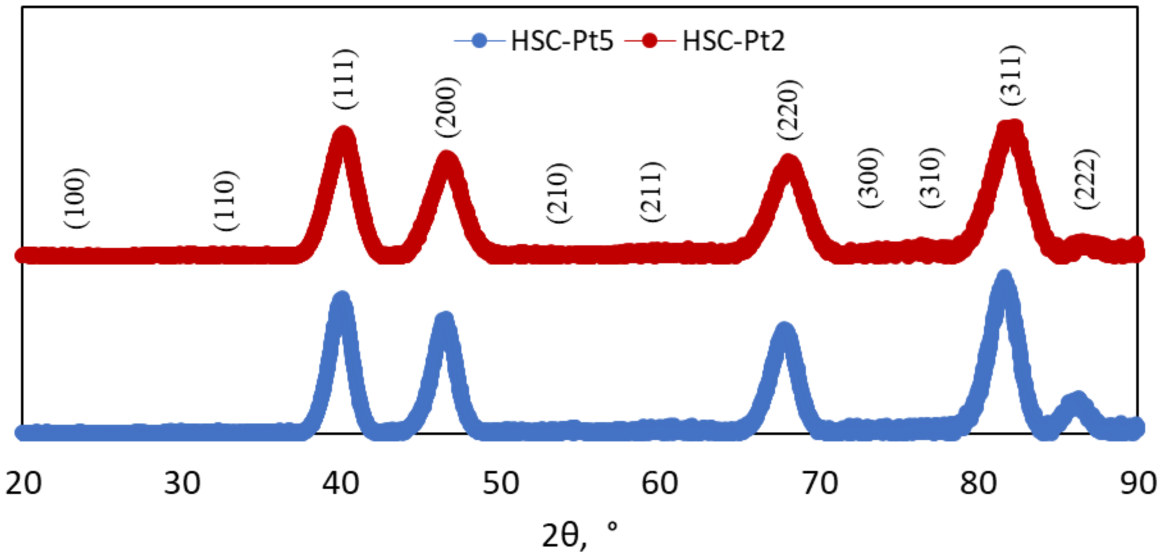

Figure 7. XRD patterns of the synthesized HSC-Pt at two different reaction temperatures: 180 °C (HSC-Pt2) and 160 °C (HSC-Pt5).

Half-cell tests are conducted to compare the electrochemical characteristics of the HSC-Pt5 and HSC-Pt2 samples. The change of the hydrogen adsorption and desorption areas for the prepared catalysts is shown in Figure 8 (a). The ECSA is calculated from the hydrogen desorption charge integrated under relevant potential range according to the hydrogen standard electrode when, on the Pt surface, adequate charge to oxidize a monolayer of hydrogen is considered as 210 μC/cm^2 [74,75].

$$ESCA = \frac{\int_{v_1}^{v_2} I\, dV}{210 * 10^{-6} * m_{pt}\ \mathrm{v}} \tag{4.3}$$

Where v_1 and v_2 are the starting and end potential (Vs RHE) of the hydrogen desorption area and m_{pt} is the actual weight of the Pt loaded onto the working electrode based on the Pt loading of the sample, v is the scan rate which is 0.1 V/s.

As it is clear from the figure, HSC-Pt2 shows higher hydrogen desorption peak, and has higher ECSA of 82.10 m^2/g, while HSC-Pt5 has ECSA of 31.08 m^2/g. Therefore, with similar Pt loading, the HSC-Pt2 sample achieves 2.64 times of ECSA compared to HSC-Pt5 by reducing the size of the Pt nanoparticles. In order to elucidate the influence of these two Pt nanoparticle sizes on the catalyst activity for ORR, both prepared catalysts are studied by running the linear sweep voltammetry (LSV) curves on rotating disk electrode at 1600 rpm under the oxygen saturated environment. As can be seen in Figure 8 (b), the current densities at onset potentials of ORR at 0.9 V for HSC-Pt2 and HSC-Pt5 are 2.85 and 2.84 mA/cm^2, respectively, and the diffusion limiting current densities are 5.69 and 6.33 mA/cm^2, respectively, at 0.3 V (Vs RHE). The higher diffusion-limiting current density at 0.3 V for HSC- Pt5 indicates that the larger sized Pt catalyst is more accessible due to less of its particles falling into the surface pores of the support HSC [76], hence relatively less resistance to reactant diffusion to the active catalytic sites [77]. On the contrary, the lower value for HSC-Pt2 is indicative of the trapping of the small Pt nanoparticles in the porous structure of the HSC support [78], which hinders their accessibility to the reactants [15]. MA and surface specific activities (SA) are calculated, at 0.9V by convention, to be 247.66 mA/mg and 301.65 $\mu A/cm^2$ for HSC-Pt2, and 212.45 mA/mg and 683.56 $\mu A/cm^2$ for HSC-Pt5, respectively. The MA represents the current per unit mass of the catalyst in 0.1 M HClO4 solution,

$$MA = \frac{J_k}{\left(\frac{m_{pt}}{A_{electrode}}\right)} \tag{4.4}$$

where m_{pt} is the actual weight of the Pt loaded onto the working electrode, $A_{electrode}$ is the area of the working electrode, which is 0.1256 cm^2, and J_k is the kinetic current density, which can be calculated using Koutecky-Levich equation (Equation 5) below.

$$\frac{1}{J} = \frac{1}{J_L} + \frac{1}{J_k} \tag{4.5}$$

where J_k is the kinetic current density, J_L is the diffusion limiting current density obtained at 0.3 V (Vs RHE) and J is the measured current density measured at 0.9 V (Vs RHE).

The SA represents the current per unit surface area of the catalyst in 0.1 M HClO4 solution,

$$SA = \frac{MA}{ECSA} \tag{4.6}$$

Combined with the XRD results, the non-spherical shape of the Pt nanoparticles of HSC-Pt5 contributes to the exposure of more active high-index planes of Pt compared to HSC-Pt2, which increases its interaction of Pt nanoparticles with support and leads to higher SA; the similar trend is also observed in other studies as well [22].

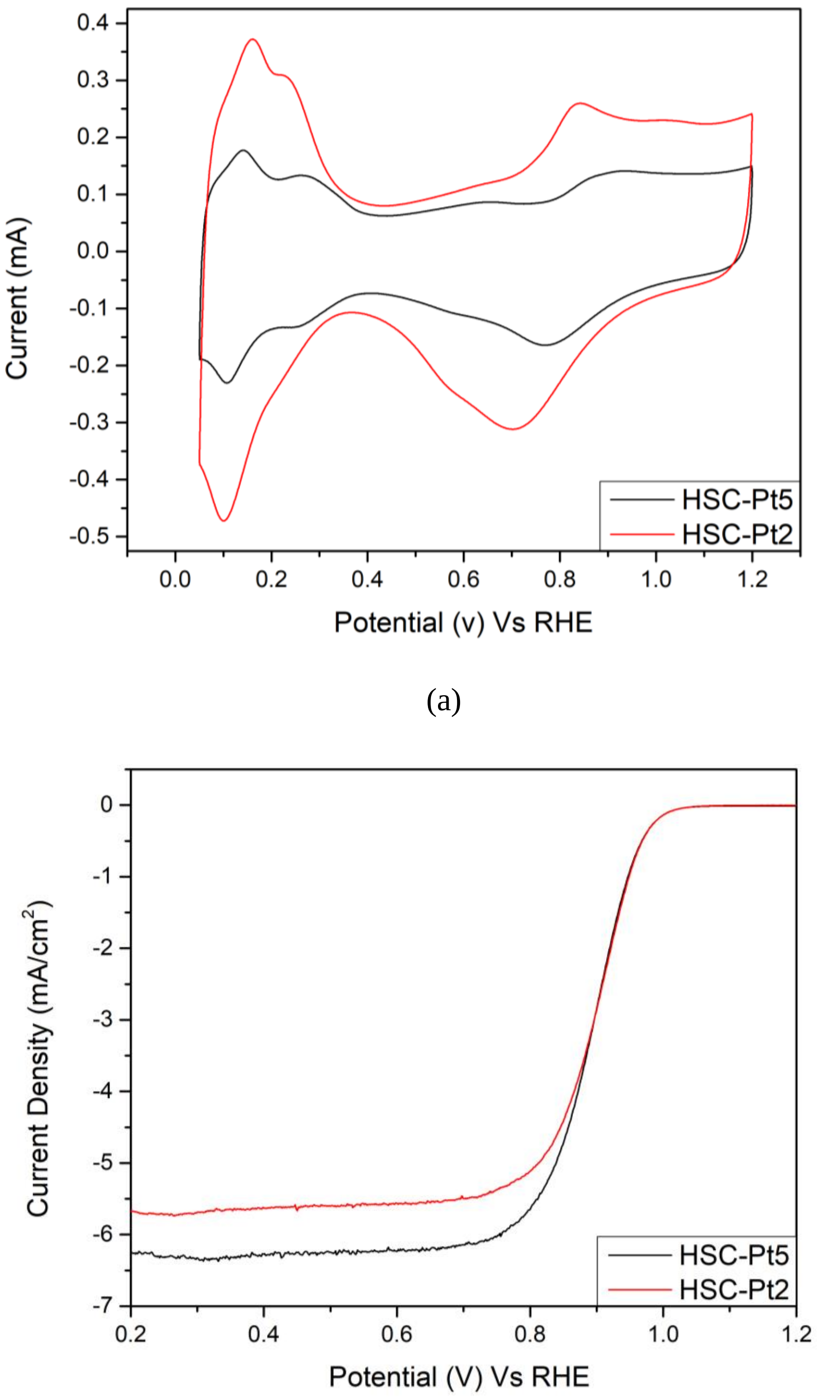

(a)

(b)

Figure 8. Half-cell electrochemical characteristics comparison between the HSC-Pt2 and HSC-Pt5: (a) cyclic voltammograms; and (b) linear sweep voltammetry at the rotation speed of 1600 rpm.

The stability of the prepared catalysts is examined using the AST. Figure 9 shows the cyclic voltammogram curves for the HSC-Pt2 and HSC-Pt5 before and after the 3,000 cycles of AST from 0.5 V to 1V at a scan rate of 0.5 V/s. It is shown that the hydrogen adsorption and desorption peaks' areas are reduced in both samples, and ECSA losses after 3,000 cycles are about 14.6 % for HSC-Pt2 and 6.0 % for HSC-Pt5. As it is seen, HSC-Pt2 has less stability than HSC-Pt5 in acidic fuel cell environment after 3,000 cycles. This can be explained by the higher surface area to volume ratio of the smaller nanoparticles, which tends to grow in size to decrease their surface free energy more easily.

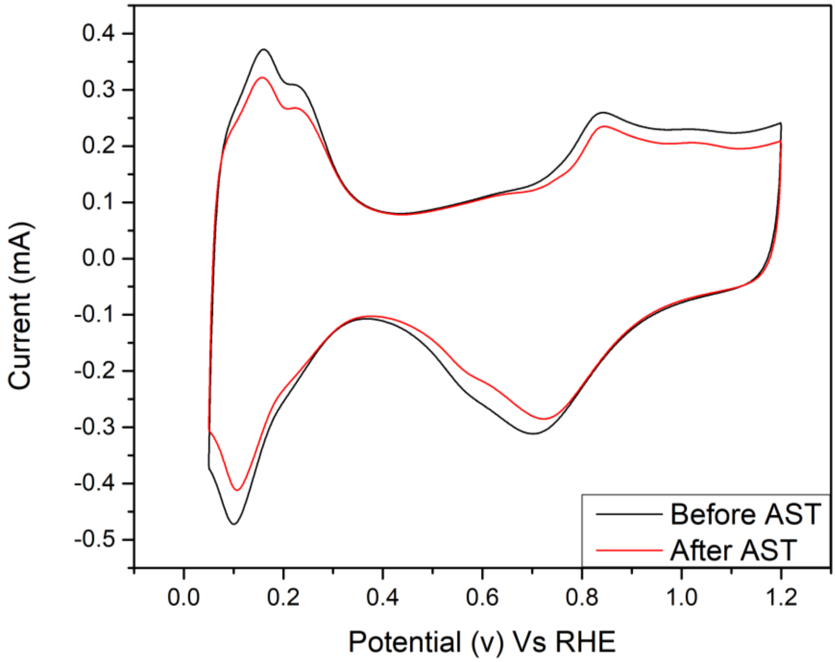

(a)

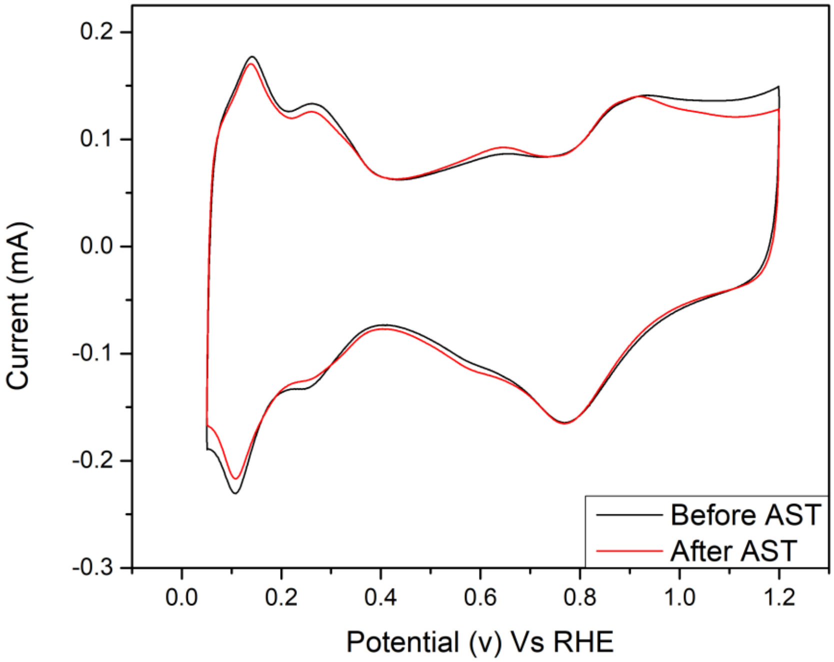

(b)

Figure 9. Half-cell electrochemical characteristics: cyclic voltammograms taken before and after the ASTs (a) HSC-Pt2 and (b) HSC-Pt5.

To evaluate the impact of the synthesized catalysts on the PEM fuel cell performance and to correlate ex-situ and in-situ electrochemical characterizations, scaled up MEAs with the active area of 45 cm^2 are prepared using the above two catalysts respectively through catalyst coated membrane method. The MEAs are tested under different operating conditions to elucidate the performances of the two catalysts. Figures 10 (a) and (b) show the polarization and power density curves of the prepared MEAs under fully humidified air and hydrogen streams. Three different flow rates – low, moderate, and high – of hydrogen and air are applied in the experiment. Hydrogen flow rates of 4.45 and air flow rates of 9 L/min are referred to as high flow, and hydrogen/air with the stoichiometric ratios of 1.2 /4 and 1.2/2 are given the name of ST 1.2-4 (moderate flow) and ST 1.2-2 (low flow), respectively. It is clear from Figure 10 (a) and (b) that both MEAs show a similar trend of variations under the different flows of reactants, and that the cell performances are improved by an increase in the reactant flows. The open circuit voltages (OCVs) are around 0.95 V under all three conditions for both MEAs. In the activation polarization regime, polarization curves are seen to be very close to each other under the different flows. For example, the cell voltage is approximately 0.85V for both MEAs when the constant current density is at 0.1 A/cm^2. The same trend is also valid for the ohmic polarization region. For instant, the cell voltage is 0.7 V for both MEAs under all three conditions when the constant current density is at 0.7 A/cm^2. However, in the concentration polarization regime, at 2.1 A/cm^2 for example, the cell voltages drop by 8% from the high flow to the low flow conditions for both MEAs. Figure 10 (c) compares the maximum power densities of both MEAs under the different flows of reactants. It can be seen that MEA made by HSC-Pt2 has a higher maximum power density than the MEA made of HSC-Pt5 under all three flows of reactants. For example, the MEA made of HSC-Pt2 shows 8% and 13% higher maximum power densities in comparison to the MEA made of HSC-5 under the high and low flow (ST 1.2-2), respectively. The higher performance of MEA made of HSC-Pt2 can be explained via the smaller size of Pt nanoparticles with a higher ratio of surface atoms leading to higher Pt surface area and utilization and may improve the accessibility of Pt nanoparticles for the constant ionomer amount.

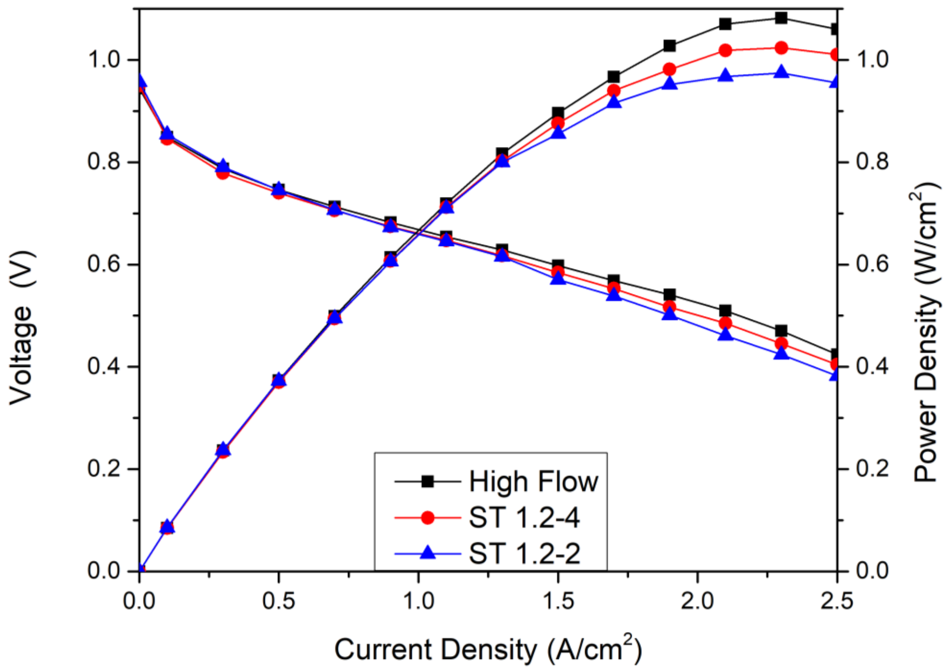

(a) HSC-Pt2

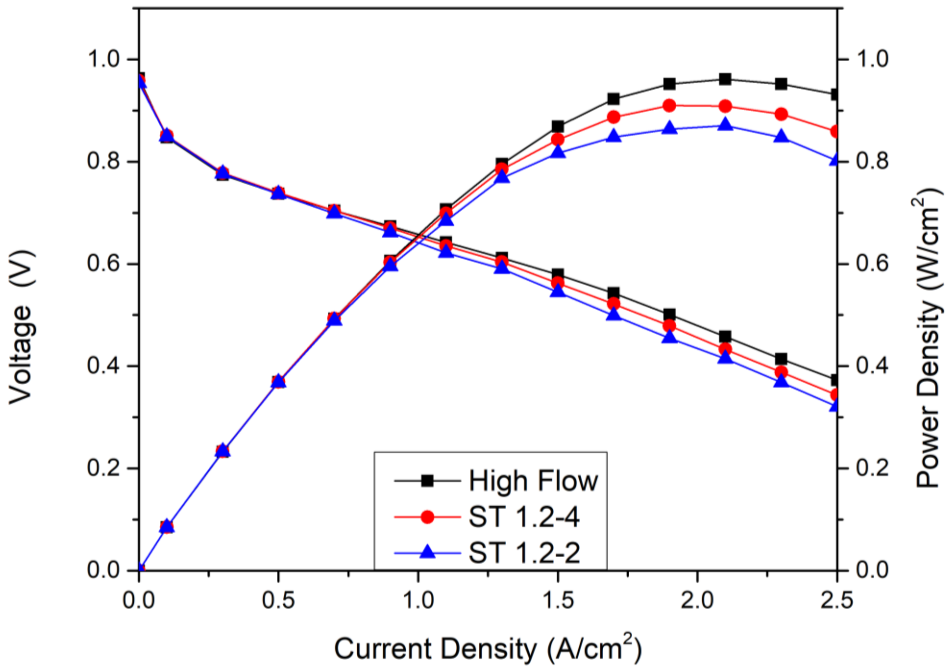

(b) HSC-Pt5

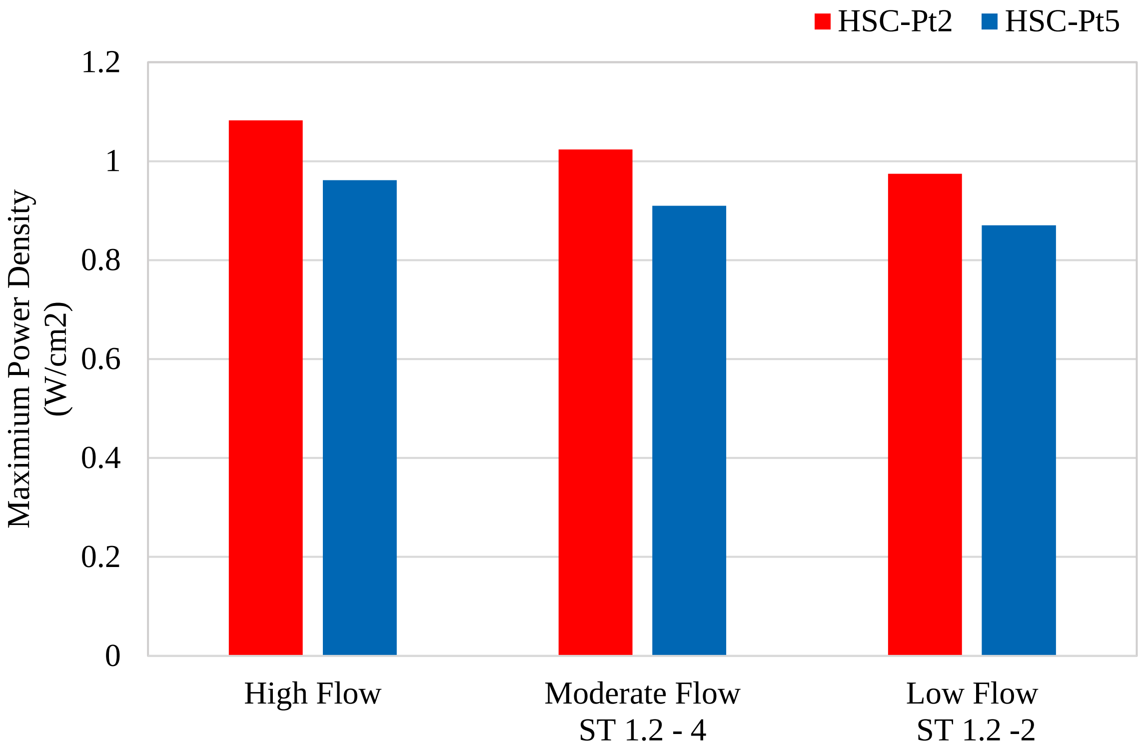

(c)

Figure 10. Polarization and power density curves obtained from the MEAs with the catalyst of (a) HSC-Pt2 and (b) HSC-Pt5 under different flow conditions of the reactants, and (c) shows the comparison of the corresponding maximum power density.

Figure 11 (a) and (b) illustrate the polarization and power density curves of the MEAs prepared with the HSC-Pt2 and HSC-Pt5 catalysts under three different flows of reactants when the RH is set at 40%. As clearly seen from the figures, both MEAs present completely different trends of variation from the results obtained under fully humidified (100% RH) condition, as the cell performance is improved by decreasing the flow of reactants. This trend of variation is significant, because higher flow rates are normally expected to provide higher accessibility of reactants, and hence increased cell performance. However, it can be seen that a high flow of reactants actually results into a poorer performance under the present low RH operation, because of dehydration in the ionic phases of the MEAs. In the activation polarization regime, both MEAs show almost the same performance, and the difference starts in the ohmic and increases in the concentration polarization regimes. As shown in the figures, the cell voltages are at about 0.81 V for both MEAs under the high flow of the reactants when the constant current density is at 0.1 A/cm^2. However, the difference becomes appreciable beyond 0.5 A/cm^2. The cell voltages are around 0.63 V and 0.61 V with the high flow of the reactants when the current density is at 0.5 A/cm^2 for MEAs made of HSC-Pt2 and HSC-Pt5, respectively. These values rise to 0.66 V and 0.65 V with the moderate flow, and 0.68 V and 0.67 V with the low flow of the reactants. The maximum power density for the MEAs made of HSC-Pt2 and HSC-Pt5, under the low flow condition, is 0.74 W/cm^2 and 0.62 W/cm^2 respectively. In addition, it can be noted that under 100% RH (See Figure 10) and 40% RH (See Figure 11), the MEA made of HSC-Pt2 shows higher performance in comparison to the MEA made of HSC-Pt5.

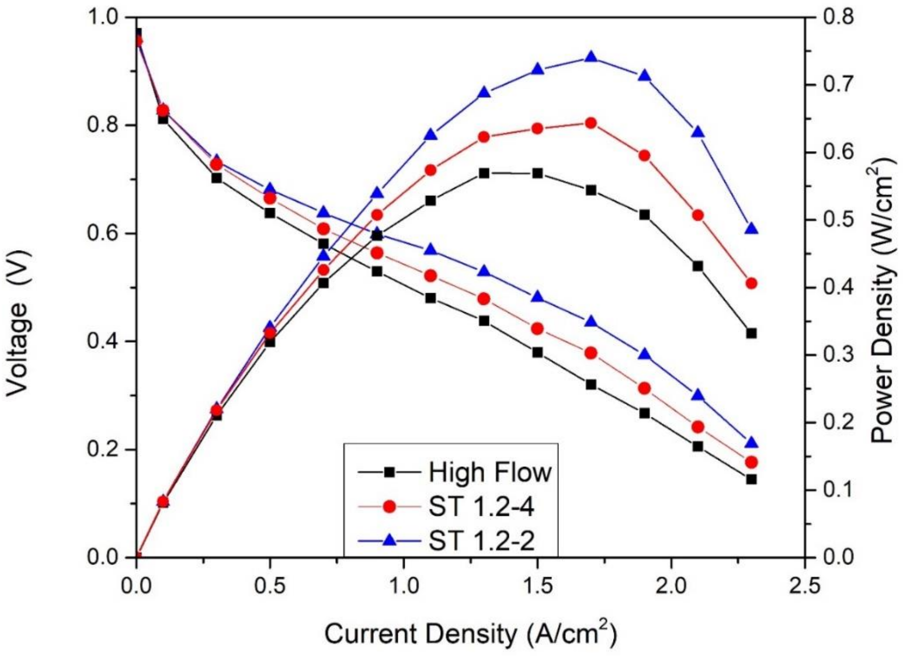

(a) HSC-Pt2

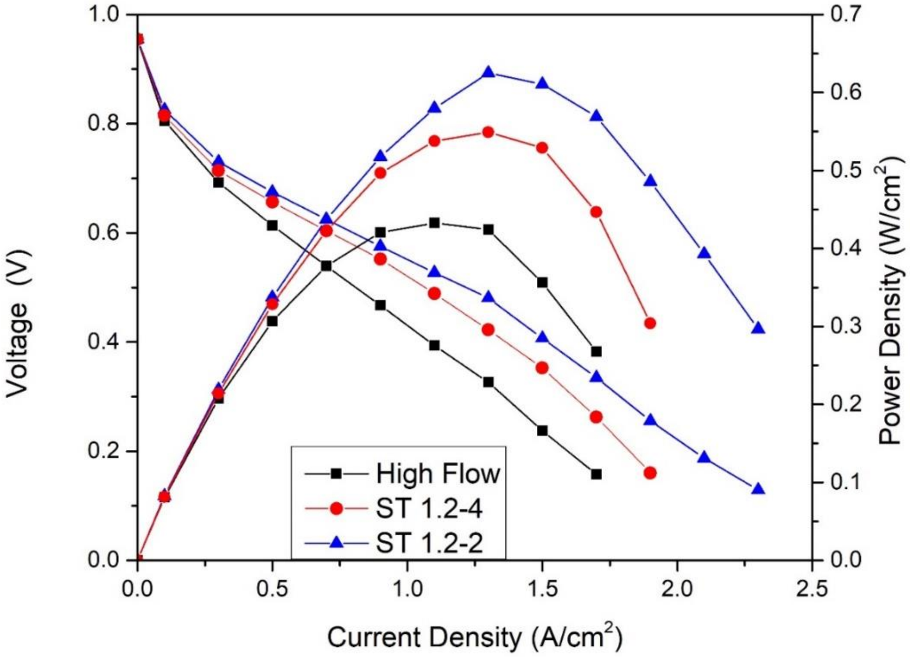

(b) HSC-Pt5

Figure 11. Polarization and power density curves by the MEAs made with (a) HSC-Pt2, (b) HSC-Pt5 under different flow conditions of the reactants, with RH of 40% at anode and cathode.

In-situ electrochemical characteristics of the MEAs prepared with HSC-Pt2 and HSC-Pt5 are presented in Figure 12. The curve shapes and hydrogen adsorption and desorption peaks are similar to those obtained in literature for MEAs prepared with commercial Pt/C catalysts [85]. It is clear that the MEA prepared with HSC-Pt2 has a higher hydrogen adsorption and desorption peaks than that with HSC-Pt5. The ECSAs are calculated based on the Pt loading, the hydrogen adsorption and desorption charges and the electrical charge associated with the monolayer adsorption of hydrogen on a Pt surface. The ECSA of the MEAs made with HSC-Pt2 and HSC-Pt5 are 73 m^2/g and 50 m^2/g, respectively.

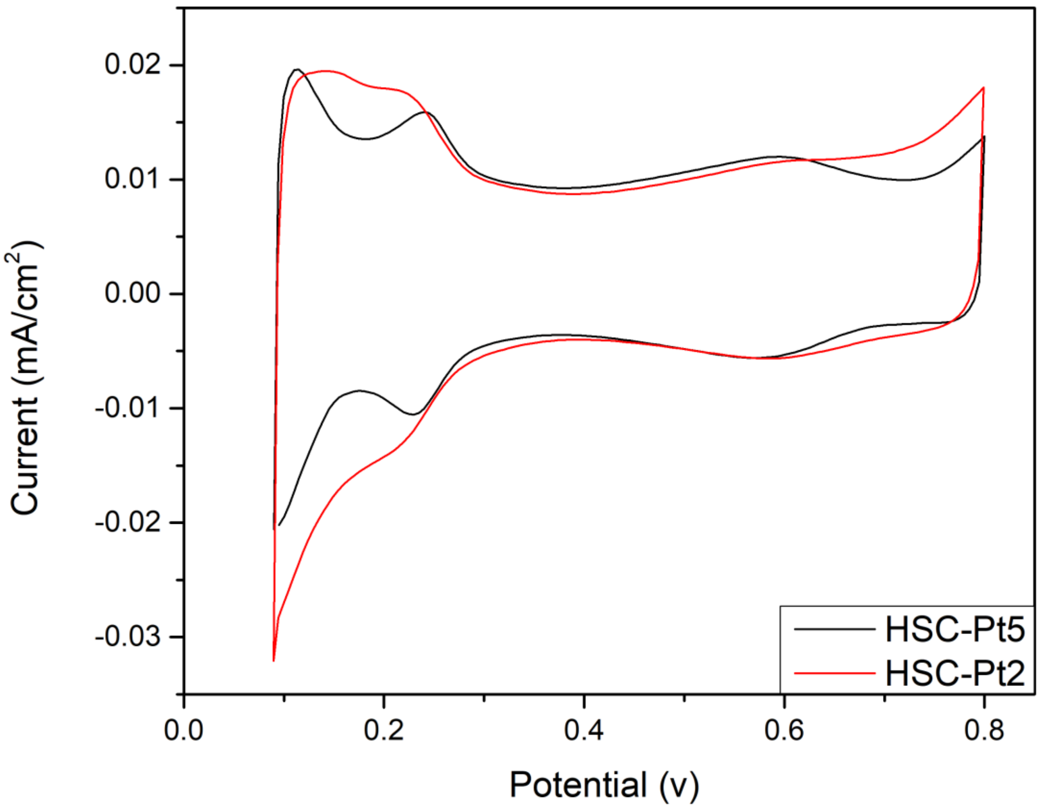

Figure 12. Cyclic voltammograms for the MEAs prepared with HSC-Pt2 and HSC-Pt5 at 75°C with back pressure of 35 kPag and RH of 100%.

Based on the ex-situ half-cell electrochemical characterizations, it is surmised that HSC-Pt2 has 164.2% higher ECSA and 16.6% higher MA over HSC-Pt5, while the SA and durability are higher for HSC-Pt5 by 116.6% and 8.6%, respectively. In addition, the scaled up single cell performance indicates 10% higher maximum power densities for MEA made of HSC-Pt2 over HSC-Pt5 under the fully humidified condition. Despite lower fuel cell performance in the MEA made of HSC-Pt5 than that of HSC-Pt2, with the maximum power densities of 0.87 W/cm^2 as compared with 0.97 W/cm^2 under the fully humidified and low flow condition, it still demonstrates very promising results when it is compared with the performance made of other synthesized and commercial catalysts reported in literature [22, 86-88]. As both the present catalysts demonstrate promising performance under different operating conditions, and half-cell data shows higher stability for HSC-Pt5, this catalyst is selected for further investigations.

In order to evaluate the loss of active surface area for MEAs made of HSC-Pt5, in-situ cyclic voltammetry is carried out, at a cell temperature of 75ºC, backpressure of 35 kPag and RH of 100%. Figure 13 (a) shows the cyclic voltammograms before and after the AST. It is clear that the hydrogen adsorption and desorption peaks are reduced after 30,000 cycles. The ECSA values are reduced by 18% after 30,000 cycles. This reduction in the electrochemical characteristics could represent 3% reduction of the open circuit voltage (OCV) values as shown in Figure 13 (b). Figure 13 (b) shows the cell performance of the MEA prepared using HSC-Pt5 before and after the AST under the identical operating condition: cell temperature of 75°C, back pressure of 35 kPag, 100% RH, and reactant flow rates of 4.45 slpm for the anode and 9 slpm for the cathode. As illustrated in the polarization curves, the OCV value slightly drops after 30,000 cycles, and the main reduction occurs in the ohmic and concentration polarization regions. For instance, when the current density is at 1.1 A/cm^2, a drop of nearly 5% in the cell voltage can be seen after 30,000 cycles. Clearly, the majority of the reduction in performance occurs in the concentration polarization regime. When the current density is at 2.1 A/cm^2, a drop of the cell voltage from 0.45 A/cm^2 to 0.39 A/cm^2 can be observed, and the maximum power density is 0.84 W/cm^2 after 30,000 AST cycles. It is worth nothing that the percentage drop of the maximum power density after AST (13%) is almost inline with the ECSA drop (18%), indicating the reduction of ECSA as the major reason for the catalyst degradation. The Nyquist plots for the MEA prepared by

HSC-Pt5 before and after the accelerated stress tests are presented in Figure 13(c). It is clear that the single impedance arc after 30,000 cycles shows higher resistance in ohmic and charge transfer area which can be related to the catalyst layer degradation and restructuring [89]. These results are well consistent with the drop in cyclic voltammograms and polarization curves.

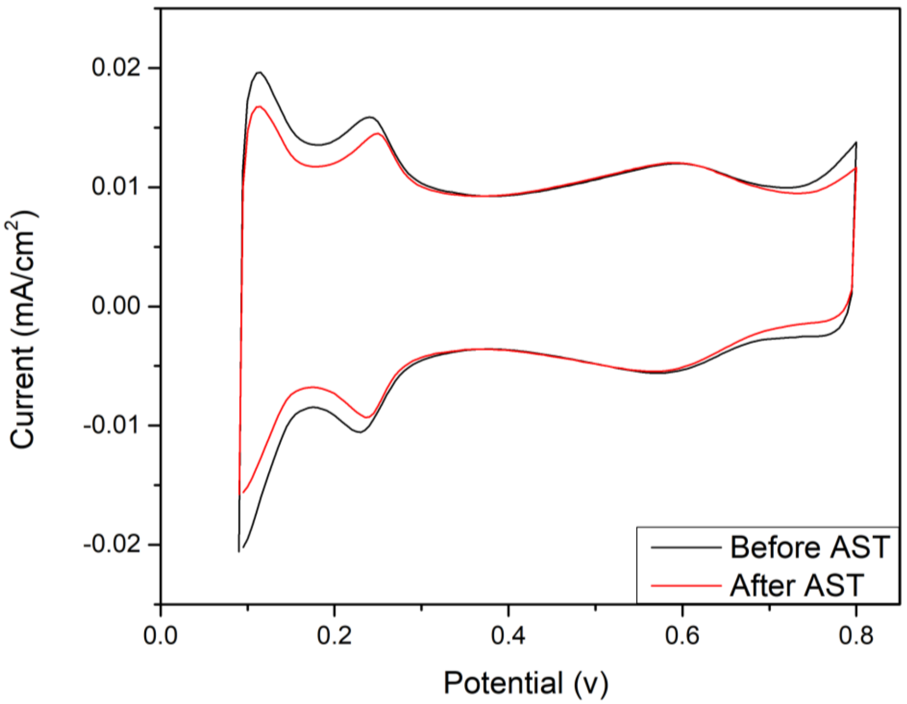

(a)

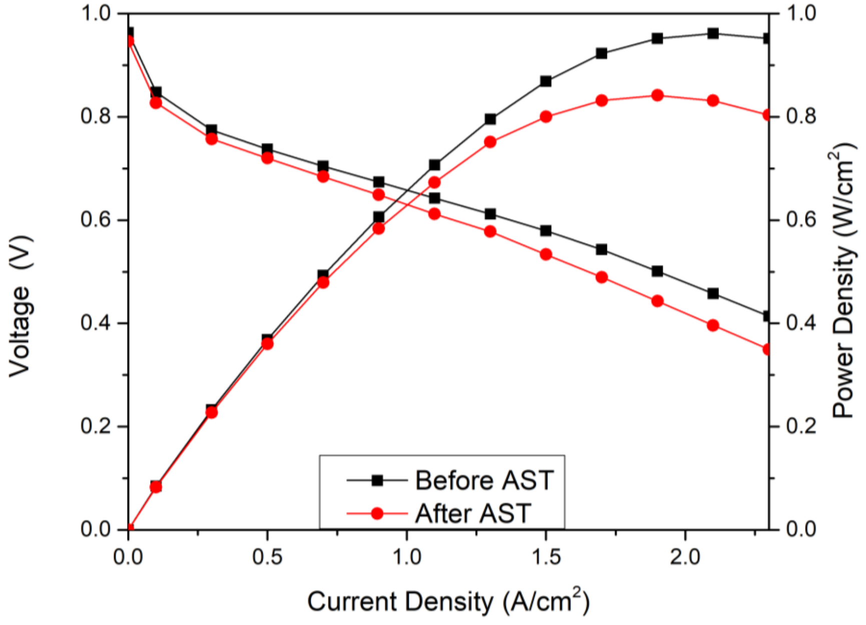

(b)

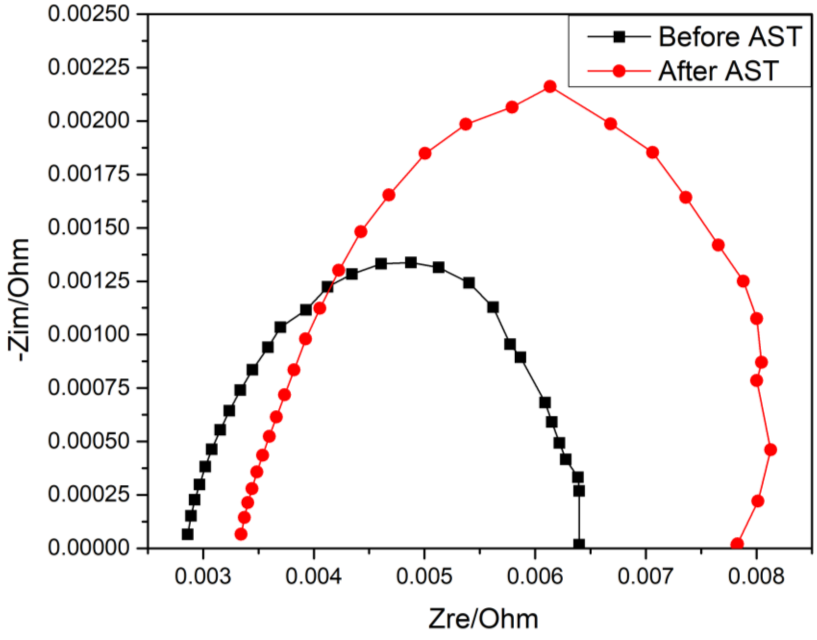

(c)

Figure 13. Electrochemical characteristics of the MEA made of HSC-Pt5, before (0 cycle) and after the AST (30,000 cycles): (a) cyclic voltammograms; (b) Polarization and power density curves; (c) Impedance

Figure 14 presents the polarization and power density curves of the MEA prepared by HSC-Pt5 before and after 30,000 cycling of AST under the low RH condition of 40%, at a cell temperature of 75ºC and backpressure of 35 kPag. As shown in the graph, the cell performances before and after the ASTs in the activation polarization regime are almost the same, and a slight decrease starts at the ohmic polarization regime, e.g., when the current density is at 0.5 A/ cm^2, the cell voltage declines by 6%. This reduction is increased in the concentration polarization regime, as the cell voltage is dropped by 37% at the current densities of 1.7 A/ cm^2. These results also demonstrate the prominent impact of the morphological and microstructural changes in the catalyst layer in single cell test which are more evident at the low RH and low flow of reactants [89]. The maximum power density is also dropped by 20% which is 7% more than the drop at the fully humidified condition. In spite of higher cell performance drop under the low RH condition, it should be noted that the maximum power density of 0.5 W/cm^2 after 30,000 cycles of AST under the low flow of reactants and partial humidification of 40% RH can be considered as excellent, and highly acceptable when compared with the cell performances reported under similar conditions in literature.

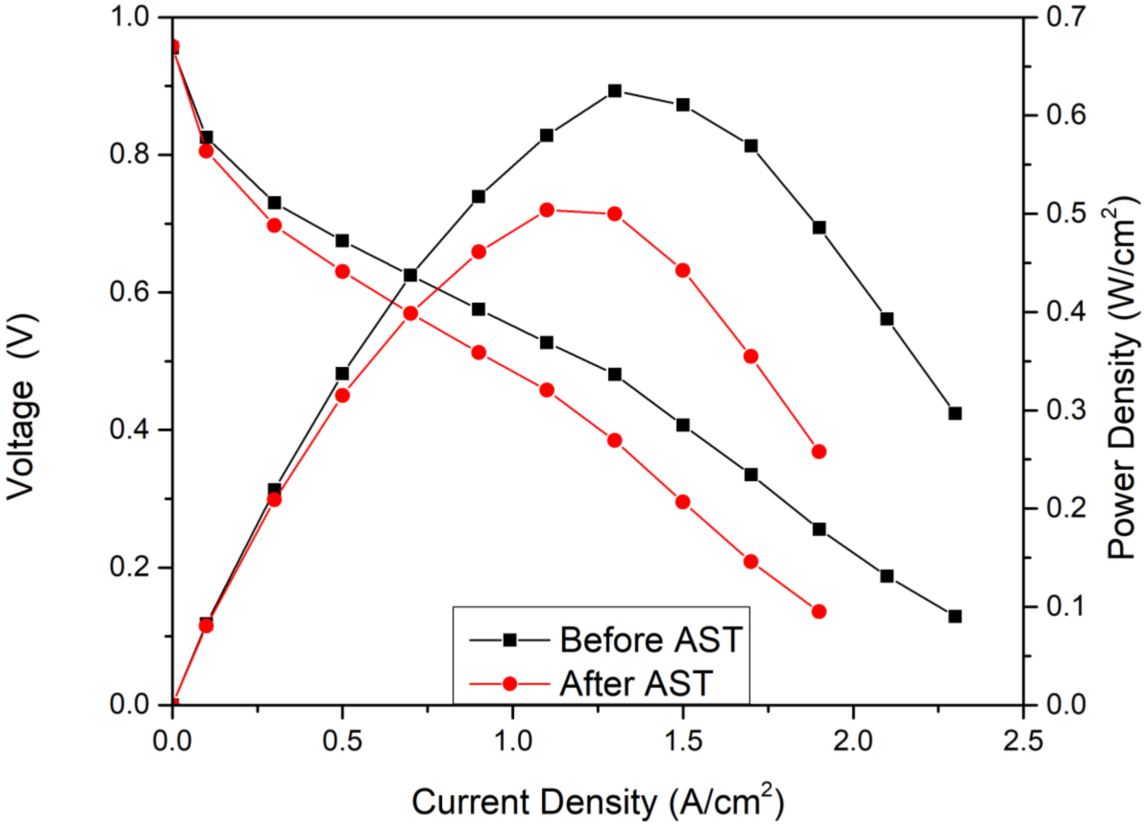

Figure 14. Polarization curves and power density curves of the MEA made of HSC-Pt5 at 40% RH and low flow ST 1.2-2 before and after AST.

Chapter 5: Conclusions and Future Work

5.1 Conclusions

In this study, one-pot synthesis method is employed for preparing the size-controlled platinum (Pt) nanoparticles on functionalized high surface area carbon (HSC). Pt nanoparticles with two different sizes of 2nm and 5nm are prepared by controlling the reaction temperature at 180 °C and 160 °C, respectively. Based on the physical characterizations, the Pt nanoparticles in both catalysts have non-spherical shapes and are well dispersed on HSC surface without any agglomeration. In addition, they have face centered cubic (fcc) crystallinity phases and are bounded with a mix of low- and high-index crystallographic planes, with total Pt loading of around 45% on HSC. The ex-situ and in-situ electrochemical characterization results, as summarized in table 2 and table 3, indicate that fuel cell performance and electrochemical surface area are strongly influenced by the size of the Pt nanoparticles. Half-cell results elucidate the prominent role of Pt nanoparticle sizes on the active surface area, mass activity and durability, while the full-cell data shows the impact of Pt nanoparticle sizes on the catalyst layer morphology and structure, and it is found that the electrochemical surface area and maximum power densities of the full cell made of the 2nm Pt nanoparticles are higher than the MEA made of the 5nm Pt nanoparticles under the different relative humidity (RH) and flow rates of reactants. Ex-situ accelerated stress tests (AST) show that HSC with 5nm particles have better durability compared to that with 2nm. In-situ AST results for the MEA prepared with the 5nm Pt nanoparticles shows 13% reduction in the maximum power density after 30,000 cycles, with the maximum power density of 0.84 W/cm^2 under the fully humidified condition; and 20% decrease with the maximum power density of 0.5 W/cm^2 after 30,000 cycles of AST under the partial humidification of 40%, illustrating the excellent performance and durability of the catalyst and the fuel cell developed in this study.

Table 2. Summary of half-cell test results

Half-cell Data	ECSA (m^2/g)	MA (mA/mg)	SA ($\mu A/cm^2$)	ECSA after AST
HSC-Pt2	82.10	247.66	301.65	70.1 (14.6% drop)
HSC-Pt5	31.08	212.45	683.56	29.2 (6.0% drop)

Table 3. Summary of single-cell test results

MEA made with	ECSA (m^2/g)	Max. Power density (W/cm^2)	Max. Power density at 40% RH (W/cm^2)	ECSA after AST	Max. Power Density After AST (W/cm^2)	Max. Power Density After AST at 40% RH (W/cm^2)
HSC-Pt2	73	1.08	0.74			
HSC-Pt5	50	0.96	0.62	41 (18% drop)	0.84 (13.4% drop)	0.51 (20% drop)

5.2 Future Work

The reliable one-pot synthesis method that has been developed to fabricate size-controlled non-spherical Pt nanoparticles, can also be further applied to the study of the impact of different support materials and/or the impact of different functionalization/doping methods on the same support material. For example, it would be interesting to combine the 3D structure of the spherical carbon back particles with 2D structures like graphene, and use the mix of the two materials as the support for Pt nanoparticles. Theoretically, the combination would benefit from the porous structure of the carbon back to get smooth transportation of both the proton and the fuel, and benefit from the extremely large active surface area from the graphene, maximizing the utilization rate of the Pt.

To further understand the impact of the size and shape of the Pt nanoparticles on the durability of the PEM fuel cell, it would be interesting to analyze the catalyst layer post the in-situ AST test. The XRD and TEM would reveal if there were any change in the shape, distribution and/or the composition of the crystallographic planes of the Pt nanoparticles, and the TGA would evaluate the potential Pt loss after the AST. However, because the limitation of the fabrication process of the MEA, during which the catalyst is coated as a thin layer directly onto the membrane surface, it can be challenging to properly collect the catalyst sample after the AST. Besides, because of the addition of the ionomer during the making of the catalyst ink, it is almost impossible to test the catalyst samples in the exact same condition as when it was prepared, reducing the value of the physical characterization results like TGA. Hence, a more comprehensive design of the experimental techniques with the focus on physical characterizations before and after the in-situ AST would be beneficial for the understanding the electrochemical characterization results and the mechanics of catalyst degradation in fuel cell environments in general.

References

[1] Ball, M. W., Ball, D., & Turner, D. S. (1965). *This fascinating oil business*. Bobbs-Merrill.

[2] Höök, M., & Tang, X. (2013). Depletion of fossil fuels and anthropogenic climate change—A review. *Energy policy*, *52*, 797-809.

[3] Bull, S. R. (2001). Renewable energy today and tomorrow. *Proceedings of the IEEE, 89*(8), 1216-1226.

[4] Erlanger, S., & Sengupta, S. (2021, July 14). Europe Unveils Plan to Shift From Fossil Fuels, Setting Up Potential Trade Spats. *The New York Times*. Retrieved August 16, 2021

[5] Gasteiger, H. A., Kocha, S. S., Sompalli, B., & Wagner, F. T. (2005). Activity benchmarks and requirements for Pt, Pt-alloy, and non-Pt oxygen reduction catalysts for PEMFCs. In *Applied Catalysis B: Environmental*.

[6] Thomas, J. M., Edwards, P. P., Dobson, P. J., & Owen, G. P. (2020). Decarbonising energy: The developing international activity in hydrogen technologies and fuel cells. *Journal of Energy Chemistry*, *51*, 405-415.

[7] GM Hydrogen Fuel Cell Vehicles. GM Heritage Center. Retrieved 24 June 2021, from https://www.gmheritagecenter.com/featured/Fuel_Cell_Vehicles.html

[8] Wang, J., Wang, H., & Fan, Y. (2018). Techno-economic challenges of fuel cell commercialization. *Engineering*, *4*(3), 352-360.

[9] Li, X. (2005). Principles of fuel cells. CRC press.

[10] Carrette, L., Friedrich, K. A., & Stimming, U. (2000). Fuel cells: principles, types, fuels, and applications. *ChemPhysChem*, *1*(4), 162-193.

[11] Wang, Y., Chen, K. S., Mishler, J., Cho, S. C., & Adroher, X. C. (2011). A review of polymer electrolyte membrane fuel cells: Technology, applications, and needs on fundamental research. *Applied energy, 88*(4), 981-1007.

[12] Freire, T. J., & Gonzalez, E. R. (2001). Effect of membrane characteristics and humidification conditions on the impedance response of polymer electrolyte fuel cells. Journal of Electroanalytical Chemistry, 503(1-2), 57-68.

[13] Nørskov, J. K., Rossmeisl, J., Logadottir, A., Lindqvist, L. R. K. J., Kitchin, J. R., Bligaard, T., & Jonsson, H. (2004). Origin of the overpotential for oxygen reduction at a fuel-cell cathode. The Journal of Physical Chemistry B, 108(46), 17886-17892.

[14] Zhang, J., Tang, Y., Song, C., & Zhang, J. (2007). Polybenzimidazole-membrane-based PEM fuel cell in the temperature range of 120–200 C. Journal of Power Sources, 172(1), 163-171.

[15] Shahgaldi, S., & Hamelin, J. (2015). Improved carbon nanostructures as a novel catalyst support in the cathode side of PEMFC: a critical review. Carbon, 94, 705-728.

[16] Zhang, J., Song, C., Zhang, J., Baker, R., & Zhang, L. (2013). Understanding the effects of backpressure on PEM fuel cell reactions and performance. Journal of Electroanalytical Chemistry, 688, 130-136.

[17] Mazúr, P., Soukup, J., Paidar, M., & Bouzek, K. (2011). Gas diffusion electrodes for high temperature PEM-type fuel cells: role of a polymer binder and method of the catalyst layer deposition. Journal of Applied Electrochemistry, 41(9), 1013-1019.

[18] Shrestha, P., Lee, C. H., Fahy, K. F., Balakrishnan, M., Ge, N., & Bazylak, A. (2020). Formation of Liquid Water Pathways in PEM Fuel Cells: A 3-D Pore-Scale Perspective. Journal of The Electrochemical Society, 167(5), 054516.

[19] Öztürk, A., Fıçıcılar, B., Eroğlu, İ., & Yurtcan, A. B. (2017). Facilitation of water management in low Pt loaded PEM fuel cell by creating hydrophobic microporous layer with PTFE, FEP and PDMS polymers: effect of polymer and carbon amounts. International Journal of Hydrogen Energy, 42(33), 21226-21249.

[20] Shao, Peles, A., & Shoemaker, K. (2011). Electrocatalysis on Platinum Nanoparticles: Particle Size Effect on Oxygen Reduction Reaction Activity. Nano Letters, 11(9), 3714–3719. https://doi.org/10.1021/nl2017459

[21] Yazici, Azder, M. A., Salihoglu, O., & Boyaci San, F. G. (2018). Ultralow Pt loading on CVD graphene for acid electrolytes and PEM fuel cells. International Journal of Hydrogen Energy, 43(40), 18572–18577. https://doi.org/10.1016/j.ijhydene.2018.06.020

[22] Xu, Zhang, H., Zhong, H., Lu, Q., Wang, Y., & Su, D. (2012). Effect of particle size on the activity and durability of the Pt/C electrocatalyst for proton exchange membrane fuel cells. Applied Catalysis. B, Environmental, 111, 264–270. https://doi.org/10.1016/j.apcatb.2011.10.007

[23] Shimazaki, Kobayashi, Y., Yamada, S., Miwa, T., & Konno, M. (2005). Preparation and characterization of aqueous colloids of Pt–Ru nanoparticles. Journal of Colloid and Interface Science, 292(1), 122–126. https://doi.org/10.1016/j.jcis.2005.05.052

[24] Whitehead, Özkar, S., & Finke, R. G. (2019). LaMer's 1950 Model for Particle Formation of Instantaneous Nucleation and Diffusion-Controlled Growth: A Historical Look at the Model's Origins, Assumptions, Equations, and Underlying Sulfur Sol Formation Kinetics Data. Chemistry of Materials, 31(18), 7116–7132. https://doi.org/10.1021/acs.chemmater.9b01273

[25] Peng, Z., & Yang, H. (2009). Designer platinum nanoparticles: Control of shape, composition in alloy, nanostructure and electrocatalytic property. Nano today, 4(2), 143-164.

[26] Chen, & Holt-Hindle, P. (2010). Platinum-Based Nanostructured Materials: Synthesis, Properties, and Applications. Chemical Reviews, 110(6), 3767–3804. https://doi.org/10.1021/cr9003902

[27] Narayanan, R., & El-Sayed, M. A. (2004). Shape-dependent catalytic activity of platinum nanoparticles in colloidal solution. Nano letters, 4(7), 1343-1348.

[28] Yin, Y., & Alivisatos, A. P. (2005). Colloidal nanocrystal synthesis and the organic–inorganic interface. Nature, 437(7059), 664-670.

[29] Calvillo, L., Gangeri, M., Perathoner, S., Centi, G., Moliner, R., & Lázaro, M. J. (2011). Synthesis and performance of platinum supported on ordered mesoporous carbons as catalyst for PEM fuel cells: effect of the surface chemistry of the support. International journal of hydrogen energy, 36(16), 9805-9814.

[30] Holby, E. F., Sheng, W., Shao-Horn, Y., & Morgan, D. (2009). Pt nanoparticle stability in PEM fuel cells: influence of particle size distribution and crossover hydrogen. Energy & Environmental Science, 2(8), 865-871.

[31] Nesselberger, M., Ashton, S., Meier, J. C., Katsounaros, I., Mayrhofer, K. J., & Arenz, M. (2011). The particle size effect on the oxygen reduction reaction activity of Pt catalysts: influence of electrolyte and relation to single crystal models. Journal of the American Chemical Society, 133(43), 17428-17433.

[32] Wikander, K., Ekström, H., Palmqvist, A. E. C., & Lindbergh, G. (2007). On the influence of Pt particle size on the PEMFC cathode performance. Electrochimica Acta, 52(24), 6848–6855.

[33] Yano, H., Watanabe, M., Iiyama, A., & Uchida, H. (2016). Particle-size effect of Pt cathode catalysts on durability in fuel cells. Nano Energy, 29, 323–333.

[34] Huang, Y., Zhang, J., Liu, Y., Subramanian, N. P., Wagner, F. T., Jorne, J., & Li, J. (2011). Transient Platinum Oxide Formation and Oxygen Reduction on Carbon-Supported Platinum and Platinum-Alloy Electrocatalysts. ECS Transactions, 41(1), 1009.

[35] Auer, E., Freund, A., Pietsch, J., & Tacke, T. (1998). Carbons as supports for industrial precious metal catalysts. Applied Catalysis A: General, 173(2), 259-271.

[36] Sharma, S., & Pollet, B. G. (2012). Support materials for PEMFC and DMFC electrocatalysts—A review. Journal of Power Sources, 208, 96-119.

[37] Uchida, M., Aoyama, Y., Eda, N., & Ohta, A. (1995). Investigation of the microstructure in the catalyst layer and effects of both perfluorosulfonate ionomer and PTFE-loaded carbon on the catalyst layer of polymer electrolyte fuel cells. Journal of the Electrochemical Society, 142(12), 4143.

[38] Antolini, E., Passos, R. R., & Ticianelli, E. A. (2002). Effects of the carbon powder characteristics in the cathode gas diffusion layer on the performance of polymer electrolyte fuel cells. Journal of Power Sources, 109(2), 477-482.

[39] Liu, Y., Ji, C., Gu, W., Jorne, J., & Gasteiger, H. A. (2011). Effects of catalyst carbon support on proton conduction and cathode performance in PEM fuel cells. Journal of The Electrochemical Society, 158(6), B614.

[40] Antolini, E. (2009). Carbon supports for low-temperature fuel cell catalysts. Applied Catalysis B: Environmental, 88(1-2), 1-24.

[41] Guha, A., Lu, W., Zawodzinski, T. A., & Schiraldi, D. A. (2007). Surface-modified carbons as platinum catalyst support for PEM fuel cells. Carbon, 45(7), 1506–1517.

[42] Ghasemi, M., Shahgaldi, S., Ismail, M., Kim, B. H., Yaakob, Z., & Daud, W. R. W. (2011). Activated carbon nanofibers as an alternative cathode catalyst to platinum in a two-chamber microbial fuel cell. International Journal of Hydrogen Energy, 36(21), 13746–13752.

[43] Zhou, Y., Neyerlin, K., Olson, T. S., Pylypenko, S., Bult, J., Dinh, H. N., ... & O'Hayre, R. (2010). Enhancement of Pt and Pt-alloy fuel cell catalyst activity and durability via nitrogen-modified carbon supports. Energy & Environmental Science, 3(10), 1437-1446.

[44] Yang, F., Xin, L., Uzunoglu, A., Qiu, Y., Stanciu, L., Ilavsky, J., ... & Xie, J. (2017). Investigation of the interaction between nafion ionomer and surface functionalized carbon black using both ultrasmall angle X-ray scattering and cryo-TEM. ACS applied materials & interfaces, 9(7), 6530-6538.

[45] Fang, Z., Lee, M. S., Kim, J. Y., Kim, J. H., & Fuller, T. F. (2020). The effect of carbon support surface functionalization on PEM fuel cell performance, durability, and ionomer coverage in the catalyst layer. Journal of The Electrochemical Society, 167(6), 064506.

[46] Klein, K. L., Melechko, A. V., McKnight, T. E., Retterer, S. T., Rack, P. D., Fowlkes, J. D., ... & Simpson, M. L. (2008). Surface characterization and functionalization of carbon nanofibers. Journal of Applied Physics, 103(6), 3.

[47] Moreno-Castilla, C., Ferro-Garcia, M. A., Joly, J. P., Bautista-Toledo, I., Carrasco-Marin, F., & Rivera-Utrilla, J. (1995). Activated carbon surface modifications by nitric acid, hydrogen peroxide, and ammonium peroxydisulfate treatments. Langmuir, 11(11), 4386-4392.

[48] Antonucci, P. L., Alderucci, V., Giordano, N., Cocke, D. L., & Kim, H. (1994). On the role of surface functional groups in Pt carbon interaction. Journal of applied electrochemistry, 24(1), 58-65.

[49] Boehm, H. P. (1994). Some aspects of the surface chemistry of carbon blacks and other carbons. Carbon, 32(5), 759-769.

[50] Kinoshita, K. (2017). Particle Size Effects for Oxygen Reduction on Highly Dispersed Platinum in Acid Electrolytes. Journal of the Electrochemical Society, 137(3).

[51] Maciá, M. D., Campiña, J. M., Herrero, E., & Feliu, J. M. (2004). On the kinetics of oxygen reduction on platinum stepped surfaces in acidic media. Journal of Electroanalytical Chemistry, 564(1–2), 141–150.

[52] Bett, J. A. S., Kinoshita, K., & Stonehart, P. (1976). Crystallite growth of platinum dispersed on graphitized carbon black: II. Effect of liquid environment. Journal of Catalysis, 41(1), 124–133.

[53] Shao, Y., Yin, G., & Gao, Y. (2007). Understanding and approaches for the durability issues of Pt-based catalysts for PEM fuel cell. Journal of Power Sources, 171(2), 558–566.

[54] Antolini, E. (2003). Formation, microstructural characteristics and stability of carbon supported platinum catalysts for low temperature fuel cells. Journal of materials science, 38(14), 2995-3005.

[55] Honji, A., Mori, T., Tamura, K., & Hishinuma, Y. (1988). Agglomeration of platinum particles supported on carbon in phosphoric acid. Journal of The Electrochemical Society, 135(2), 355.

[56] Guilminot, E., Corcella, A., Charlot, F., Maillard, F., & Chatenet, M. (2006). Detection of Pt z+ ions and Pt nanoparticles inside the membrane of a used PEMFC. Journal of The Electrochemical Society, 154(1), B96.

[57] Xie, J., Wood, D. L., Wayne, D. M., Zawodzinski, T. A., Atanassov, P., & Borup, R. L. (2004). Durability of PEFCs at high humidity conditions. Journal of the Electrochemical Society, 152(1), A104.

[58] Blurton, K. F., Kunz, H. R., & Rutt, D. R. (1978). Surface area loss of platinum supported on graphite. Electrochimica Acta, 23(3), 183-190.

[59] Ferreira, P. J., Shao-Horn, Y., Morgan, D., Makharia, R., Kocha, S., & Gasteiger, H. A. (2005). Instability of Pt ⁄ C electrocatalysts in proton exchange membrane fuel cells: a mechanistic investigation. Journal of the Electrochemical Society, 152(11), A2256.

[60] Campbell, C. T., Parker, S. C., & Starr, D. E. (2002). The effect of size-dependent nanoparticle energetics on catalyst sintering. Science, 298(5594), 811–814.

[61] Wilson, M. S., Garzon, F. H., Sickafus, K. E., & Gottesfeld, S. (1993). Surface area loss of supported platinum in polymer electrolyte fuel cells. Journal of the Electrochemical Society, 140(10), 2872.

[62] Borup, R. L., Davey, J. R., Garzon, F. H., Wood, D. L., & Inbody, M. A. (2006). PEM fuel cell electrocatalyst durability measurements. Journal of Power Sources, 163(1 SPEC. ISS.), 76–81.

[63] Delime, F., & Lamy, C. (1998). Optimization of platinum dispersion in Pt–PEM electrodes: application to the electrooxidation of ethanol. Journal of applied electrochemistry, 28(1), 27-35.

[64] Bing, Y., Liu, H., Zhang, L., Ghosh, D., & Zhang, J. (2010). Nanostructured Pt-alloy electrocatalysts for PEM fuel cell oxygen reduction reaction. Chemical Society Reviews, 39(6), 2184-2202.

[65] Vitos, L., Ruban, A. V., Skriver, H. L., & Kollár, J. (1998). The surface energy of metals. Surface science, 411(1-2), 186-202.

[66] Chen, J., Lim, B., Lee, E. P., & Xia, Y. (2009). Shape-controlled synthesis of platinum nanocrystals for catalytic and electrocatalytic applications. Nano Today, 4(1), 81-95.

[67] Stamenkovic, V. R., Fowler, B., Mun, B. S., Wang, G., Ross, P. N., Lucas, C. A., & Markovic, N. M. (2007). Improved oxygen reduction activity on Pt3Ni (111) via increased surface site availability. science, 315(5811), 493-497.

[68] Quan, Z., Wang, Y., & Fang, J. (2013). High-index faceted noble metal nanocrystals. Accounts of Chemical Research, 46(2), 191-202.

[69] Tian, N., Zhou, Z. Y., Sun, S. G., Ding, Y., & Wang, Z. L. (2007). Synthesis of tetrahexahedral platinum nanocrystals with high-index facets and high electro-oxidation activity. science, 316(5825), 732-735.

[70] Lee, W. H., & Kim, H. (2013). Electrocatalytic activity and durability study of carbon supported Pt nanodendrites in polymer electrolyte membrane fuel cells. international journal of hydrogen energy, 38(17), 7126-7132.

[71] Huang, R., Wen, Y. H., Zhu, Z. Z., & Sun, S. G. (2011). Structure and stability of platinum nanocrystals: from low-index to high-index facets. Journal of Materials Chemistry, 21(31), 11578-11584.

[72] Veizaga, N., Fernandez, J., Bruno, M., Scelza, O., & De Miguel, S. (2012). Deposition of Pt nanoparticles on different carbonaceous materials by using different preparation methods for PEMFC electrocatalysts. International Journal of Hydrogen Energy, 37(23), 17910–17920.

[73] Moghaddam, R. B., Shahgaldi, S., & Li, X. (2017). A facile synthesis of high activity cube-like Pt/carbon composites for fuel cell application. Frontiers in Energy, 11(3), 245–253.

[74] Shahgaldi, S., & Hamelin, J. (2015). The effect of low platinum loading on the efficiency of PEMFC's electrocatalysts supported on TiO2–Nb, and SnO2–Nb: an experimental comparison between active and stable conditions. Energy Conversion and Management, 103, 681–690.

[75] Zhang, J. (2008). PEM fuel cell electrocatalysts and catalyst layers: fundamentals and applications. Springer Science & Business Media.

[76] Pollet, B. G. (2009). A novel method for preparing PEMFC electrodes by the ultrasonic and sonoelectrochemical techniques. Electrochemistry Communications, 11(7), 1445–1448.

[77] Vinayan, B. P., Jafri, R. I., Nagar, R., Rajalakshmi, N., Sethupathi, K., & Ramaprabhu, S. (2012). Catalytic activity of platinum–cobalt alloy nanoparticles decorated functionalized multiwalled carbon nanotubes for oxygen reduction reaction in PEMFC. International Journal of Hydrogen Energy, 37(1), 412–421.

[78] Yaldagard, M., Jahanshahi, M., & Seghatoleslami, N. (2013). Carbonaceous nanostructured support materials for low temperature fuel cell electrocatalysts—a review. World Journal of Nano Science and Engineering, 2013.

[79] Sriring, N., Tantavichet, N., & Pruksathorn, K. (2010). Preparation of Pt/C catalysts by electroless deposition for proton exchange membrane fuel cells. Korean Journal of Chemical Engineering, 27(2), 439–445.

[80] Shinozaki, K., Zack, J. W., Richards, R. M., Pivovar, B. S., & Kocha, S. S. (2015). Oxygen reduction reaction measurements on platinum electrocatalysts utilizing rotating disk electrode technique I. Impact of impurities, measurement protocols and applied corrections. Journal of The Electrochemical Society, 162(10), F1144–F1158.

[81] Gilman, S. (1963). A STUDY OF THE MECHANISM OF CARBON MONOXIDE ADSORPTION ON PLATINUM BY A NEW ELECTROCHEMICAL PROCEDURE1. The Journal of Physical Chemistry, 67(1), 78–84.

[82] Leonard, N., Nallathambi, V., Barton, S.C. (2013) Carbon supports for non-precious metal oxygen reducing catalysts. Journal of The Electrochemical Society 160 (2013) F788-F792.

[83] Zhao, J., Ozden, A., Shahgaldi, S., Alaefour, I. E., Li, X., & Hamdullahpur, F. (2018). Effect of Pt loading and catalyst type on the pore structure of porous electrodes in polymer electrolyte membrane (PEM) fuel cells. Energy, 150, 69-76.

[84] Wang, S., Chen, S., Ma, L., & Zapien, J. A. (2021). Recent Progress in Cobalt-based Carbon Materials as Oxygen Electrocatalysts for Zinc-Air Batteries Applications. Materials Today Energy, 100659.

[85] Kumpulainen, H., Peltonen, T., Koponen, U., Bergelin, M., Valkiainen, M., & Wasberg, M. (2002). In situ voltammetric characterization of PEM fuel cell catalyst layers. Technical Research Centre of Finland. Research Notes, 2137, 28."

[86] Mohsin, M., Raza, R., Mohsin-ul-Mulk, M., Yousaf, A., & Hacker, V. (2019). Electrochemical characterization of polymer electrolyte membrane fuel cells and polarization curve analysis. International Journal of Hydrogen Energy."

[87] Hsieh, S., & Su, Y. (2014). Effects of anode and cathode perforated flow field plates on proton exchange membrane fuel cell performance. International Journal of Energy Research, 38(7), 944–953."

[88] Jung, J.-H., Cha, M.-S., & Kim, J.-B. (2012). Optimization of nafion ionomer content using synthesized Pt/carbon nanofibers catalyst in polymer electrolyte membrane fuel cell. Journal of Nanoscience and Nanotechnology, 12(7), 5412–5417."

[89] Shahgaldi, S., Ozden, A., Li, X., & Hamdullahpur, F. (2020). A scaled-up proton exchange membrane fuel cell with enhanced performance and durability. Applied Energy, 268, 114956.